J. Fluid Mech. (2010), *vol.* 653, *pp.* 137–173.
doi:10.1017/S0022112010000212

Non-Newtonian fluid displacements in horizontal narrow eccentric annuli: effects of slow motion of the inner cylinder

M. CARRASCO-TEJA[1] AND I. A. FRIGAARD[1,2]†

[1]Department of Mathematics, University of British Columbia, 1984 Mathematics Road, Vancouver, BC, Canada V6T 1Z2

[2]Department of Mechanical Engineering, University of British Columbia, 2054-6250 Applied Science Lane, BC, Canada V6T 1Z4

(Received 7 July 2009; revised 10 January 2010; accepted 12 January 2010)

We study non-Newtonian fluid displacements in horizontal narrow eccentric annuli in the situation where the inner cylinder is moving. This represents a practically important extension of the model analysed by Carrasco-Teja *et al.* (*J. Fluid Mech.*, vol. 605, 2008, pp. 293–327). When motion of the inner cylinder is included, the Hele-Shaw model closure becomes significantly more complex and extremely costly to compute, except for Newtonian fluids. In the first part of the paper we address the model derivation and closure relations. The second part of the paper considers the limit of large buoyancy number, in which the interface elongates along the annulus. We derive a lubrication-style model for this situation, showing that the leading-order interface is symmetric. Rotation of the inner cylinder only affects the length of the leading-order interface, and this occurs only for non-Newtonian fluids via shear-thinning effects. At first order, casing rotation manifests in an asymmetrical 'shift' of the interface in the direction of the rotation. We also derive conditions on the eccentricity, fluid rheology and inner cylinder velocity, under which we are able to find steady travelling wave displacement solutions.

1. Introduction

The aim of this paper is to understand the effects of slow casing motion on non-Newtonian fluid displacements in horizontal narrow eccentric annuli. This may be interpreted as a sequel to Carrasco-Teja *et al.* (2008), in which we have studied this type of displacement flow, for the case in which the walls of the annulus are fixed. In this situation we were able to find conditions on the dimensionless rheological parameters, annulus eccentricity and (small) angle of inclination from horizontal, under which a steady travelling wave displacement front could exist. Such displacements correspond to a 100 % efficient displacement. In other situations the displacement is less efficient: the interface is found to elongate progressively during the displacement. When the displacement fluids have a yield stress, a more severe situation arises in which a fluid may get stuck on the narrow side of the annulus (see McLean, Manry & Whitaker 1966), in which case the displacement is never complete. The principal motivation for the study of Carrasco-Teja *et al.* (2008) came from the industrial

† Email address for correspondence: frigaard@math.ubc.ca

process of primary cementing, which involves displacement of non-Newtonian fluids along narrow eccentric annuli. The process is described at length in Nelson & Guillot (2006). See figure 1 below for a schematic of the process.

In the industrial process, the fluids are drilling muds, spacer fluids, washes and cement slurries, which have a broad range of rheological properties. The annular space is formed by the borehole wall and the outer wall of a steel casing that is inserted into the newly drilled borehole. The casing slumps downwards under gravity, so that the annuli are eccentric. This space is occupied by drilling fluid which must be removed before the cement is placed, so as to ensure a good bond of the cement with the annular walls and a tight hydraulic seal. Drilling fluids are usually non-Newtonian and often possess a yield stress, which can lead to fluids getting stuck on the narrow side of the annulus. In the past 20 years there has been a massive increase in the number of horizontal wells constructed worldwide, primarily to increase productivity by aligning the well with the reservoir. The early 1990s saw a continual pushing of the horizontal extent of wells up to around 10 km (see e.g. the detailed description in Payne, Wilton & Ramos 1995). The 10 km barrier was broken in a number of wells drilled at Wytch Farm, UK, around 2000. The limits of 'extreme' extended reach wells are now being pushed into the 15–20 km range, but such wells are unusual and do not necessarily bring productivity benefits proportional to their technical challenges. In the present day, it is routinely feasible to construct wells with horizontal extensions in the 7–10 km range.

Although many of the potential problems of cementing horizontal wells were identified some time ago (see e.g. Sabins 1990), the industrial response has been largely through technological advances, rather than by developing understanding of physical fundamentals that may affect the process. In longer horizontal wells it is increasingly common to have laminar flows, both due to smaller annular gap sizes and to the increased risk of high frictional pressures fracturing the surrounding formation at high flow rates. In the absence of a density difference between fluids, displacements in horizontal annuli are the same as in vertical annuli. However, drilling fluids are typically 100–600 kg m^{-3} lighter than cement slurries, and a chemically compatible spacer fluid designed to have intermediate density and rheological properties typically separates these two fluids. This means that significant density differences are always present in the cementing of horizontal wells.

In Carrasco-Teja *et al.* (2008) we answered a number of questions, of both fluid mechanic interest and of practical industrial relevance. Which dimensionless groups govern whether or not the flow will become stratified? With a density difference, is it possible to have steady, travelling wave, displacement fronts? What are the effects of an increased flow rate on a horizontal displacement? In this paper, which is still motivated by primary cementing displacements, we consider motion of the inner cylinder in the annulus. In the industrial setting it is becoming common to slowly rotate and/or reciprocate the inner cylinder, which is called the 'casing'. The precise effects of casing movement is unknown, but the underlying reasoning is to forcibly shear the drilling mud, so as to ease displacement on the narrow side of the annulus. This objective is probably achieved: the walls of the annulus are fairly rough, so that slip is unlikely, and therefore imposing relative motion must yield the fluid. What is unknown however, are the wider effects of casing motion on these displacement flows. Developing this understanding is the objective of our study.

The flows that we consider are laminar and the annuli considered have annular gaps that are narrow with respect to both circumferential and axial length scales. Thus, a Hele-Shaw modelling approach is appropriate and we adapt such an approach to

the case of casing motion. The underlying idea of using a Hele-Shaw/porous media approach to model these displacements dates back to Martin, Latil & Vetter (1978) and Tehrani, Ferguson & Bittleston (1992), but was put in the present formulation by Bittleston, Ferguson & Frigaard (2002). We first restrict the model of Bittleston *et al.* (2002) to a uniform annular section of constant inclination, eccentricity and radii, then incorporate both rotation and axial motion of the inner cylinder.

The principal difficulty in developing the Hele-Shaw approach in this direction is computational. At their heart, Hele-Shaw (and related) methods rely on being able to solve a reduced two-dimensional shear flow, in the plane of the flow, then averaging the velocity across the narrow gap. The closure relation developed in this way relates the gap-averaged velocity field to the modified pressure gradient (i.e. Darcy's law in the porous media context), and is used to eliminate either the pressure or the stream function from the governing equations. In the absence of wall motion, this closure relation can be expressed analytically, even for non-Newtonian fluids of the types commonly used.

With a moving wall, the underlying shear flow is a two-dimensional planar Poiseuille–Couette flow, for which the closure relations are only calculable analytically in the case of Newtonian fluids. For Newtonian fluids therefore, development of a displacement model with wall motion is quite straightforward, leading to an elliptic linear two-dimensional partial differential equation for the stream function. Although rheological aspects are missing, at least some characteristics of displacements with casing motion can be understood by a Newtonian model, and this we have developed in Carrasco-Teja & Frigaard (2009). For non-Newtonian fluids, we formulate the underlying displacement model in this paper. However, to solve a fully two-dimensional displacement flow problem for such fluids is not attempted. The field equation for the stream function is still elliptic, but now is nonlinear, and to resolve the nonlinearity at each point in space requires numerical solution of the underlying local planar Poiseuille–Couette flow solution. Iteration is needed both for this local closure and for the elliptic field equation. The computational task is thus formidable.

The results from Carrasco-Teja & Frigaard (2009), on Newtonian fluid displacements are interesting. First of all, it has been possible to find steady-state travelling wave solutions for concentric and mildly eccentric annuli, in the presence of casing motion. These solutions are developed via a domain perturbation method, that relies on the leading-order interface being almost perpendicular to the direction of gravity. This occurs only when the buoyancy number of the flow is small. The buoyancy number $\tilde{b}$ reflects the ratio of static pressure difference (over the scale of the annular gap), to the principal viscous stresses. Although convenient to have such analytical solutions, small buoyancy number is relatively unusual in cementing. In Carrasco-Teja & Frigaard (2009) we have shown numerically that in fact steady displacements also occur far away from the strict domain of validity of the assumptions needed for analytical solution.

Casing rotation reduces the extension of the interface in the axial direction, and also results in an azimuthal phase shift of the steady shape away from a symmetrical profile. The phase shift results in the positioning of heavy fluid over light fluid along segments of the interface. When the axial extension of the interface is sufficiently large this leads to a local buoyancy driven fingering instability. A simple theory is developed by Carrasco-Teja & Frigaard (2009) for this type of fingering. Over longer times, the local fingering is replaced by steady propagation of a diffuse interfacial region that may spread slowly due to dispersion. Slow axial motion of the annulus walls on its own is apparently less interesting. There is no breaking of the symmetry

of the interface and hence no instability. However, axial wall motion does generate secondary flows which may combine with those from inner cylinder rotation resulting in enhanced dispersive effects. The numerical regimes explored by Carrasco-Teja & Frigaard (2009) are restricted to small and $O(1)$ buoyancy number.

The large buoyancy number regime was studied Carrasco-Teja *et al.* (2008), but for a stationary casing (annulus with fixed walls). At large $|\tilde{b}|$, buoyancy effects dominate and the interface slumps under gravity as it advances. The slump distance scales with $|\tilde{b}| \gg 1$, which prompted the development of a lubrication style displacement model by Carrasco-Teja *et al.* (2008). This approach not only leads to analytical results (discussed earlier) but also is sensible computationally in avoiding computing over long-thin domains. Later, in the second part of this paper, we develop a similar lubrication model approach, but now including motion of the inner cylinder.

Other than the work reviewed above, the model of Bittleston *et al.* (2002) has been extensively studied in Pelipenko & Frigaard (2004*a*,*b*,*c*), for near vertical annuli. As with horizontal displacements, the dynamics are dominated by the existence (or not) of steady travelling wave solutions, i.e. for certain parameter values the displacement front advects along the annulus at the mean pumping speed. Analytic solutions to the displacement problem, exhibiting the steady travelling wave behaviour, are constructed by Pelipenko & Frigaard (2004*a*) and investigated numerically by Pelipenko & Frigaard (2004*b*). It is also possible to predict the domains of existence of steady and unsteady displacements using a lubrication-style displacement model (see Pelipenko & Frigaard 2004*c*). A time-dependent version of the Hele-Shaw part of the model was developed in Moyers-González *et al.* (2007) and used to investigate interfacial instabilities in Moyers-González & Frigaard (2008, 2009).

There are also a limited number of computational studies of annular displacement flows which do not follow the Hele-Shaw approach. Szabo & Hassager (1995, 1997), have computed a three-dimensional immiscible displacement flow between two Newtonian fluids using the arbitrary Lagrange–Euler formulation. The model shows reasonable agreement with a film-draining model derived for concentric annular displacements and also shows that the displacement efficiency drops significantly with annular eccentricity. Three-dimensional approaches have also been taken by other authors, using general purpose computational fluid dynamics (CFD) codes, e.g. Jakobsen *et al.* (1991); Vefring *et al.* (1997); Dutra *et al.* (2004); Nguyen *et al.* (2008). As with Szabo & Hassager (1995, 1997), such studies have value in understanding details of the flow near the interface but are of limited use in understanding flows on a larger scale, which is the advantage of the Hele-Shaw approach. A hybrid two-dimensional/three-dimensional approach has recently been adopted by Savery, Darbe & Chin (2007), in which the Navier–Stokes equations are simplified by ignoring radial velocities and azimuthal pressure gradients, but the model is still resolved in three dimensions. The authors are able to include casing motion in this approach, but a justification of the assumptions and even details of the final simplified model are not given in Savery *et al.* (2007).

An outline of our paper is as follows. In § 2 we present the Hele-Shaw model including casing motion. Two formulations of the model are given: one based on a concentration equation and one with a clean interface (more suitable for analytical work). We also discuss the closure problem, in § 2.1.1 and later in more depth in the Appendix. Displacements at large buoyancy number are considered in § 3. We first use the Newtonian displacement model from Carrasco-Teja & Frigaard (2009) to demonstrate that long interfaces, of length $\sim O(|\tilde{b}|)$, also occur in the presence of casing motion, i.e. as for the stationary casing situation in Carrasco-Teja *et al.* (2008).

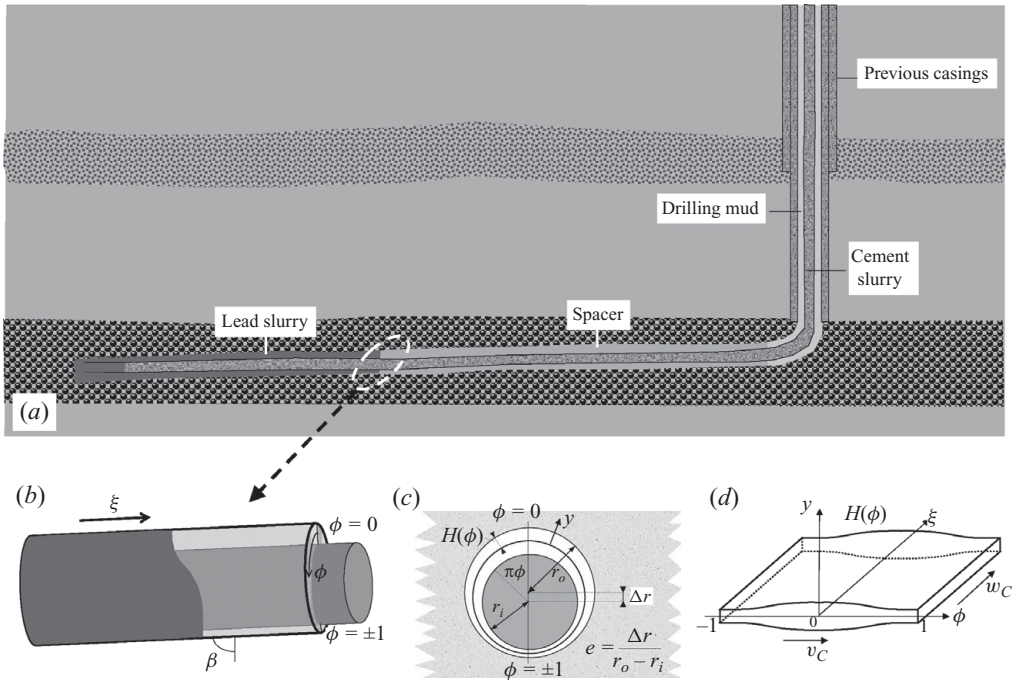

FIGURE 1. Schematic of the process geometry: (*a*) primary cementing of a horizontal well, (*b*) narrow eccentric annulus, (*c*) annular cross-section, (*d*) unwrapped annulus/periodic Hele-Shaw cell.

We then derive a lubrication-style displacement model for the interfacial region of such flows, which results in a quasi-linear advection–diffusion equation for the interface position(s). We simplify the analysis using a perturbation procedure, which shows that the leading-order interface position is symmetric, with a rotational asymmetric 'shift' occurring at first order. In § 4 we address the key question of whether or not steady travelling wave solutions are possible. We provide conditions that are necessary and sufficient for the lubrication model to have steady solutions, and explore solutions for typical parameter ranges in Newtonian, power law and Bingham fluid models. The paper closes with a brief discussion of the results in § 5.

2. Model outline

The model derivation that we adopt follows closely that in Bittleston *et al.* (2002) (see also Pelipenko & Frigaard 2004*a*; Carrasco-Teja *et al.* 2008; Carrasco-Teja & Frigaard 2009). We consider displacement flows in a nearly-horizontal narrow eccentric annulus, in which the inner cylinder may slowly translate and/or rotate. We use a coordinate system (y, ϕ, ξ), as illustrated in figure 1: y measures radial distance from the centreline of the annular gap, $\phi \in [-1, 1]$ denotes a scaled azimuthal coordinate and ξ measures distance along the annulus. The geometry is described by the eccentricity e, angle of inclination to the vertical β and annular gap width,

$$2H(\phi) \approx 2(1 + e\cos\pi\phi),$$

i.e. $y \in [-H(\phi), H(\phi)]$. The inner cylinder is rotating at a dimensionless speed v_C, and reciprocating with a velocity w_C. The underlying model we shall derive is a Hele-Shaw

style model, with now the added complication that the inner wall of the eccentric annular Hele-Shaw cell is moving.

We adopt the convention of denoting all dimensional quantities with a $\hat{\cdot}$, and dimensionless quantities without. Scaling and model reduction follows the steps in Bittleston *et al.* (2002) and Carrasco-Teja *et al.* (2008). The narrowness of the annular gap is measured using the aspect ratio: $\delta = (\hat{r}_o - \hat{r}_i)/[\pi(\hat{r}_o + \hat{r}_i)]$, where $\hat{r}_o$ and $\hat{r}_i$ are inner and outer cylinder radii, respectively. A Reynolds number for the displacement is defined as $Re = [\hat{\rho}^* \hat{w}^* (\hat{r}_o - \hat{r}_i)]/\hat{\mu}^*$, where $\hat{\mu}^*$ and $\hat{\rho}^*$ are suitable density and viscosity scales, and $\hat{w}^*$ is the mean axial velocity. As is usual for Hele-Shaw models, the basic assumptions used in the derivation are that $\delta \ll 1$ and $\delta Re \ll 1$. A summary of scaling and dimensionless numbers may be found in § 2.3.

As before, we work with two formulations for the model: (i) a fluid concentration-based formulation, which is effective for computational simulation; (ii) an interface tracking formulation which is more convenient for analytical work. The fluid concentration formulation is considered in the large-Péclet-number limit, in which diffusion/dispersion is neglected, and the two models are formally equivalent.

2.1. *Fluid concentration formulation*

The velocity components in (y, ϕ, ξ) directions are denoted (u, v, w), and to leading order the mass-conservation equation is

$$\frac{\partial u}{\partial y} + \frac{\partial v}{\partial \phi} + \frac{\partial w}{\partial \xi} = 0. \tag{2.1}$$

To eliminate the radial velocity, we average across the gap width, using conditions of no-slip at the annulus walls to get

$$\frac{\partial}{\partial \phi}[H\bar{v}] + \frac{\partial}{\partial \xi}[H\bar{w}] = 0, \tag{2.2}$$

where $(\bar{v}, \bar{w})$ are the averaged velocity components in the (ϕ, ξ) directions, i.e.

$$\bar{v} = \frac{1}{2H}\int_{-H}^{H} v \, \mathrm{d}y, \quad \bar{w} = \frac{1}{2H}\int_{-H}^{H} w \, \mathrm{d}y. \tag{2.3}$$

The two key assumptions made in this modelling approach are (i) that the fluid concentration c is uniform across the narrow annular gap; (ii) that diffusion/dispersion may be neglected. The reader is referred to Bittleston *et al.* (2002) for a discussion of these assumptions. Making these assumptions allows us to derive the following leading-order equation for the gap-averaged fluid concentration $\bar{c}$:

$$\frac{\partial}{\partial t}[H\bar{c}] + \frac{\partial}{\partial \phi}[H\bar{v}\,\bar{c}] + \frac{\partial}{\partial \xi}[H\bar{w}\,\bar{c}] = 0. \tag{2.4}$$

Note that under the assumptions made, $\bar{c} = c$, but for consistency with our previous work we use the notation $\bar{c}$. The fluids are modelled as Herschel–Bulkley fluids. The dimensionless density, consistency, power law index and yield stress of pure fluid k are denoted respectively by ρ_k, κ_k, n_k and $\tau_{k,Y}$, for $k = 1, 2$. In the concentration-based formulation, fluid properties at intermediate concentrations are modelled via closure expressions involving the above pure fluid properties and $\bar{c}$, i.e. we write simply $\rho(\bar{c})$, $\kappa(\bar{c})$, $n(\bar{c})$ and $\tau_Y(\bar{c})$ for these closures. For simple displacements (e.g. pure fluid 1 displaces pure fluid 2 at given flow rate with an initially 'sharp' interface), intermediate concentrations only arise local to the interface, due to numerical diffusion/dispersion effects. We have not found that the precise closure relationships used have a significant

effect on such displacements and consequently have used only linear interpolation of the fluid properties.

Only the gap-averaged velocity and concentration appear in (2.2) and (2.4), which are valid in the two-dimensional domain $(\phi, \xi) \in [-1, 1] \times [0, L]$, where typically $L \gg 1$. To provide closure of this system we derive the leading-order momentum equations, using the typical scaling arguments of Hele-Shaw models. The pressure does not vary across the annular gap and the reduced momentum equations in (ϕ, ξ) directions are

$$\frac{\partial \tau_{\phi y}}{\partial y} = -G_\phi, \tag{2.5}$$

$$\frac{\partial \tau_{\xi y}}{\partial y} = -G_\xi, \tag{2.6}$$

where $\boldsymbol{G} = (G_\phi, G_\xi)$ is the modified pressure gradient field, given by

$$\boldsymbol{G} = \left(-p_\phi + \frac{\rho \sin\beta \sin\pi\phi}{St^*}, -p_\xi - \frac{\rho \cos\beta}{St^*} \right). \tag{2.7}$$

Here St^* is the Stokes number for the flow, which is defined below in § 2.3, where we also summarize the scaling used and other dimensionless groups. The scaled leading-order constitutive model is

$$\tau_{\phi y} = \eta \frac{\partial v}{\partial y} \Longleftrightarrow \tau > \tau_Y, \tag{2.8}$$

$$\tau_{\xi y} = \eta \frac{\partial w}{\partial y} \Longleftrightarrow \tau > \tau_Y, \tag{2.9}$$

$$\dot{\gamma} = 0 \Longleftrightarrow \tau \leqslant \tau_Y, \tag{2.10}$$

where $\tau = (\tau_{\phi y}^2 + \tau_{\xi y}^2)^{1/2}$, the leading-order rate of strain second invariant is

$$\dot{\gamma} = \left(\frac{\partial v}{\partial y}^2 + \frac{\partial w}{\partial y}^2 \right)^{1/2},$$

and the effective viscosity is

$$\eta = \kappa \dot{\gamma}^{n-1} + \frac{\tau_Y}{\dot{\gamma}}. \tag{2.11}$$

The remainder of the model derivation proceeds along standard lines. Firstly, we define the gap-averaged velocity in terms of a stream function Ψ:

$$2H\bar{w} = \frac{\partial \Psi}{\partial \phi}, \quad 2H\bar{v} = -\frac{\partial \Psi}{\partial \xi}. \tag{2.12}$$

Secondly, we derive the closure relationship between $\boldsymbol{G}$ and the gap-averaged velocity $\overline{\boldsymbol{u}} = (\overline{v}, \overline{w})$ (or equivalently $\nabla\Psi$). Thirdly, we cross differentiate $\boldsymbol{G}$ to eliminate the pressure, which leads to an elliptic problem for the stream function Ψ:

$$\nabla \cdot \boldsymbol{S} = -\nabla \cdot \boldsymbol{f} \tag{2.13}$$

where $\boldsymbol{S} = (G_\xi, -G_\phi)$ and where the buoyancy terms manifest in the term

$$\boldsymbol{f} = \rho(\overline{\boldsymbol{c}}) \left(\frac{\cos\beta}{St^*}, \frac{\sin\beta \sin\pi\phi}{St^*} \right). \tag{2.14}$$

Boundary conditions for (2.13) are

$$\Psi(\phi + 2, \xi) = \Psi(\phi, \xi) + 4, \tag{2.15}$$

$$\frac{\partial \Psi}{\partial \xi} = -H v_C, \text{ at } \xi = 0,\ L. \tag{2.16}$$

The first of these ensures that the mean axial velocity is equal to 1, which follows from our choice of scaling. The second ensures that in the far field, away from the interface, the azimuthal flow is given by the Couette component due to the moving casing.

2.1.1. *Remarks on the formulation and closure relations*

As is usual in this kind of two-dimensional model, there is the option of eliminating either the pressure from the system and working with the stream function or vice versa. When the casing is moving, the fluids are sheared and the mapping from $\boldsymbol{G}$ to $\overline{\boldsymbol{u}}$ is one to one. Thus either formulation could be used. However, for a stationary casing, the mapping from $\overline{\boldsymbol{u}}$ to $\boldsymbol{G}$ is not uniquely defined at $\overline{\boldsymbol{u}} = 0$ for yield stress fluids. Physically, a finite range of modified pressure gradients $\boldsymbol{G}$ fail to mobilize a yield stress fluid, i.e. whenever $|\boldsymbol{G}| \leqslant \tau_Y / H$ we have $\overline{\boldsymbol{u}} = 0$. This has led, in Bittleston *et al.* (2002) and our other work, to the adoption of the stream function formulation. For consistency of approach we retain the stream function formulation here for the moving casing.

The main difference between this and the stationary casing models that we have worked with before is in the closure relation, between $\boldsymbol{G}$ and $\overline{\boldsymbol{u}}$, or equivalently between $\nabla\Psi$ and $\boldsymbol{S}$. This closure is derived by solving the simplified momentum equations, (2.5) and (2.6), at each (ϕ, ξ), subject to boundary conditions:

$$(v, w) = (v_C, w_C) \text{ at } y = -H(\phi), \quad (v, w) = (0, 0) \text{ at } y = H(\phi).$$

For a Newtonian fluid we derive straightforwardly the linear relations:

$$\boldsymbol{G} = \frac{3\kappa}{H^2}\left(\overline{\boldsymbol{u}} - \frac{1}{2}(v_C, w_C)\right), \tag{2.17}$$

$$\boldsymbol{S} = \frac{3\kappa}{2H^3}\left(\nabla\Psi - H(w_C, -v_C)\right), \tag{2.18}$$

separating Poiseuille and Couette effects.

For the non-Newtonian fluids that we consider there is no fully analytical solution available if the casing velocity is non-zero. For stationary casing, there is an implicit relationship between $\nabla\Psi$ and $\boldsymbol{S}$, that is derived in Bittleston *et al.* (2002). For a moving casing, the closure may be computed reasonably quickly and it is also possible to derive certain qualitative results. These results are derived fully in the Appendix, but here we mention just three results that are useful later.

(*a*) For fixed (v_C, w_C), the constant vector $\boldsymbol{G}$ uniquely defines $\overline{\boldsymbol{u}}$ (or equivalently $\boldsymbol{S}$ uniquely defines $\nabla\Psi$).

(*b*) If $\nabla\Psi_1$ is defined by $\boldsymbol{S}_1$ and $\nabla\Psi_2$ is defined by $\boldsymbol{S}_2$, the following monotonicity result holds:

$$[\nabla\Psi_1 - \nabla\Psi_2] \cdot [\boldsymbol{S}_1 - \boldsymbol{S}_2] \geqslant 0. \tag{2.19}$$

(*c*) Defining the jth moment of the mobility, m_j by

$$m_j = \int_{-H}^{H} \left(\frac{y}{H}\right)^j \frac{1}{\eta}\, \mathrm{d}y. \tag{2.20}$$

The following relationships are satisfied:

$$\overline{\boldsymbol{u}} = \frac{1}{2}(v_C, w_C)\left(1 + \frac{m_1}{m_0}\right) + H^2\left(m_2 - \frac{m_1^2}{m_0}\right)\boldsymbol{G}, \tag{2.21}$$

$$\nabla\Psi = H(w_C, -v_C)\left(1 + \frac{m_1}{m_0}\right) + 2H^3\left(m_2 - \frac{m_1^2}{m_0}\right)\boldsymbol{S}. \tag{2.22}$$

The first of these results, (*a*), ensures that we have a closure to compute. The second of these, (*b*), can be exploited to ensure uniqueness of the stream function solution to (2.13). It also allows us to compute the closure in different ways. In fact, provided that (v_C, w_C) is non-zero the fluid is sheared and the inequality in (2.19) is strict (as can be verified numerically). This means that, for example, we may do any of (i) specify $\nabla\Psi$ and compute $\boldsymbol{S}$; (ii) specify $\boldsymbol{S}$ and compute $\nabla\Psi$; (iii) specify both Ψ_ϕ and S_ξ, and compute Ψ_ξ and S_ϕ; (iv) specify both Ψ_ξ and S_ϕ, and compute Ψ_ϕ and S_ξ. This allows for considerable flexibility that we shall later exploit.

The third of the properties given above, (*c*), shows that, although the mobility moments m_j do need to be computed numerically, there is a well-defined splitting into Couette and Poiseuille components directly analogous to (2.17) and (2.18). Note that in the case of a Newtonian fluid, $m_1 = 0$, $m_2 = 1/(3\kappa)$, and (2.17) and (2.18) are recovered. In the case of a pure Couette flow the stress is constant across the annular gap and hence $m_1 = 0$. Finally, it is worth noting that the expression $(m_2 - m_1^2/m_0) > 0$, from the Cauchy–Schwarz inequality, except in the degenerate case where $m_j = 0, \forall j$, which corresponds to the fluid being unyielded throughout the channel and is not possible for non-zero (v_C, w_C).

2.2. *Interface tracking formulation*

In this formulation the domain is divided into two fluid domains: Ω_1 for the displacing fluid 1, and Ω_2 for the displaced fluid 2, in each of which (2.13) is replaced by

$$\nabla \cdot \boldsymbol{S}_1 = 0, \quad (\phi, \xi) \in \Omega_1, \tag{2.23}$$

$$\nabla \cdot \boldsymbol{S}_2 = 0, \quad (\phi, \xi) \in \Omega_2, \tag{2.24}$$

with $\boldsymbol{S}_k$ defined exactly as $\boldsymbol{S}$ is defined for the concentration dependent formulation, but with properties ρ_1, $\tau_{1,Y}$, κ_1, n_1 in fluid 1 and ρ_2, $\tau_{2,Y}$, κ_2, n_2 in fluid 2. Note that for constant density ρ_k, we have that $\nabla \cdot \boldsymbol{f}_k = 0$, hence the right-hand side of (2.23) and (2.24). If the interface is denoted by $\phi = \phi_i(\xi, t)$, this satisfies the kinematic condition

$$\frac{\partial \phi_i}{\partial t} + \bar{w}\frac{\partial \phi_i}{\partial \xi} = \bar{v}, \tag{2.25}$$

which essentially replaces the concentration advection equation. The leading-order continuity conditions at the interface are that the stream function Ψ and the pressure p are continuous across the interface. Assuming sufficient regularity of the interface, the former condition assures that the normal velocity, the derivative of Ψ along the interface, is well defined at the interface. Pressure continuity is expressed in terms of defining the jump in $\boldsymbol{S}_k$ across the interface:

$$\left[\left(S_{k,\xi}\frac{\partial \phi_i}{\partial \xi} - S_{k,\phi}\right) + \left(\frac{\rho_k \sin\beta \sin\pi\phi}{St^*}\frac{\partial \phi_i}{\partial \xi} - \frac{\rho_k \cos\beta}{St^*}\right)\right]_1^2 = 0. \tag{2.26}$$

Effectively this is $[(\boldsymbol{S}_k + \boldsymbol{f}_k) \cdot \boldsymbol{n}]_1^2 = 0$.

2.3. *Summary of scaling and dimensionless numbers*

All parameters and variables used above are dimensionless, and our results will be presented in terms of dimensionless quantities. Our dimensionless model contains the following 13 dimensionless parameters.

(i) Eccentricity: $e \in [0, 1)$, which is defined in figure 1(c).

(ii) Angle of inclination: β, as illustrated in figure 1(b).

(iii) Azimuthal casing speed: $v_C = 0.5\pi(\hat{r}_o + \hat{r}_i)\hat{\Omega}_C/\hat{w}^*$, where $\hat{r}_o$ and $\hat{r}_i$ are the outer and inner radii of the annulus, $\hat{\Omega}_C$ is the angular velocity of the inner cylinder and $\hat{w}^*$ is the mean velocity, defined in terms of the imposed flow rate $\hat{Q}$ by $\hat{Q} = \pi(\hat{r}_o^2 - \hat{r}_i^2)\hat{w}^*$. Note that typically $|v_C| < 1$.

(iv) Axial casing speed: $w_C = \hat{w}_C/\hat{w}^*$, and typically $|w_C| < 1$.

(v) Fluid j power-law index: n_j. Typically the fluids are shear thinning, so $n_j \leqslant 1$.

(vi) Fluid j yield stress: $\tau_{j,Y} = \hat{\tau}_{j,Y}/\hat{\tau}^*$, where $\hat{\tau}^* = \max_{k=1,2}\{\hat{\tau}_{k,Y} + \hat{\kappa}_k[\hat{\dot{\gamma}}^*]^{n_k}\}$, is a viscous stress scale defined using $\hat{\dot{\gamma}}^* = 2\hat{w}^*/(\hat{r}_o - \hat{r}_i)$, as a representative strain rate. Note that by definition, $\tau_{j,Y} \leqslant 1$.

(vii) Fluid j consistency: $\kappa_j = \hat{\kappa}_j[\hat{\dot{\gamma}}^*]^{n_k}/\hat{\tau}^*\}$. Note that by definition, $\kappa_j \leqslant 1$.

(viii) Fluid j density: $\rho_j = \hat{\rho}_j/\max_{k=1,2}\{\hat{\rho}_k\}$, so that one of the densities is $= 1$ and the other is $\leqslant 1$, representing the density ratio. Here $\hat{\rho}_j$ is the dimensional density of fluid j.

(ix) Stokes number: $St^* = [2\hat{\tau}^*]/[\max_{k=1,2}\{\hat{\rho}_k\}\hat{g}(\hat{r}_o - \hat{r}_i)]$, where $\hat{g}$ is the gravitational acceleration.

This is a formidable set of parameters, but there are some restrictions in range, as indicated. Firstly, we shall consider inclinations that are close to $\beta = \pi/2$. Secondly, we shall always consider that the heavier fluid displaces the lighter fluid, i.e. $\rho_1 = 1$, $\rho_2 < 1$. Thirdly, if we consider only the pure fluid properties and assume that the phases are advected without any diffusion/dispersion, the fluid density only enters the picture via buoyancy and always combines with the Stokes number. The effects of buoyancy are characterized by the dimensionless parameter, $\tilde{b} = (\rho_2 - \rho_1)/St^*$:

$$\tilde{b} = \frac{\rho_2 - \rho_1}{St^*} = \frac{(\hat{\rho}_2 - \hat{\rho}_1)\hat{g}(\hat{r}_o - \hat{r}_i)}{2\hat{\tau}^*}, \tag{2.27}$$

clearly representing the ratio of buoyant to viscous forces. Note that since the displacing fluid is assumed heavier here, $\tilde{b} < 0$. In Carrasco-Teja & Frigaard (2009) we have considered $|\tilde{b}| = O(1)$, mostly numerically, and for Newtonian fluids only. Here we shall explicitly consider the limit of $|\tilde{b}| \gg 1$, in which we also allow deviations from a horizontal annulus, with angles $|\beta - \pi/2| \sim O(1/|\tilde{b}|)$. Thus, the main dimensionless parameters governing this limit are the eccentricity e, the dimensionless casing speeds, v_C and w_C and the six rheological parameters (all bounded above by 1).

The dimensionless casing speeds are of $O(1)$ partly for practical reasons. The casing is moved primarily in order to ensure that any gel in the drilling mud is broken. Large values of w_C mean a rapid reciprocation which is impractical over length scales of hundreds of metres driven mechanically from the surface. Note that a value $w_C > 2$ would mean that the Couette component of velocity (driven by pulling the casing) is faster than the mean pumping velocity, which is very unlikely. Similarly, we should note that large rotation rates may result in shearing of the casing and/or some component of the drive mechanism, both of which are difficult and expensive to remedy downhole. From the mathematical perspective, in deriving the Hele-Shaw model we would require that the casing speeds are of the same order as the mean

flow velocity. In this paper we assume that the casing speeds are constant, but this is not strictly necessary. Suitably slow variations in time would not affect the model derivation (and as the well is finite in length the axial speed must vary in time, i.e. the casing is reciprocated).

To recover dimensional quantities from the reduced model, the axial and azimuthal velocities have been scaled with the mean flow velocity $\hat{w}^*$ axial and azimuthal lengths with the half-circumference, $0.5\pi(\hat{r}_o + \hat{r}_i)$, and time with $0.5\pi(\hat{r}_o + \hat{r}_i)/\hat{w}^*$.

The principal assumptions made in the derivation are those standard for Hele-Shaw approaches, i.e. $\delta \ll 1$ and $\delta Re \ll 1$ (see earlier for the definitions). These are the main physical limitations, to ensure that inertia and other stress components are absent. Additionally, we have assumed that concentration variations across the gap are minimal. Otherwise we would need to model diffusive and dispersive effects with the concentration.

3. Displacements at high buoyancy numbers

The model described in the previous section is derived for laminar displacement flows in horizontal annuli with arbitrary casing motion and rheological parameters. As discussed in § 2.1.1 the main complexity of the model comes in the closure between $\nabla\Psi$ and $\boldsymbol{S}$. This complexity arises due to casing motion, which imposes a Couette component and means that the modified pressure gradient is no longer parallel to the gap-averaged velocity field. In Carrasco-Teja & Frigaard (2009) the Newtonian version has been solved computationally, which simply consists of a linear elliptic equation for the stream function, coupled to (2.4) for the concentration. For non-Newtonian fluids we could adapt the Augmented Lagrangian approach used in Pelipenko & Frigaard (2004*b*); Carrasco-Teja *et al.* (2008), but having to evaluate the underlying model closures numerically makes this task extremely slow numerically. Therefore, we instead consider a limiting set of flows that allows further model simplification, i.e. the limit $|\tilde{b}| \gg 1$.

3.1. *Example Newtonian simulations for* $|\tilde{b}| \gg 1$

In fixed casing flows at large $|\tilde{b}|$, Carrasco-Teja *et al.* (2008) have observed that the displacement front typically elongates along the annulus for a distance of $O(|\tilde{b}|)$. The elongated front may either propagate as a steady travelling wave, moving at the mean displacement velocity, or may spread further if the rheological parameters do not allow for a stable steady travelling wave solution. We explore whether this situation also occurs in the presence of casing motion, using the model and computational method detailed in Carrasco-Teja & Frigaard (2009), for Newtonian fluid displacements.

Figure 2 presents results from Newtonian computations with a 4:1 viscosity ratio and small eccentricity at $\tilde{b} = -50$. Three simulations are presented at increasing casing rotation rates, with no axial casing velocity. The parameters are chosen so that at $v_C = 0$ there exists a steady travelling wave solution, according to the conditions developed in Carrasco-Teja *et al.* (2008), and this is confirmed numerically. We observe that for modest increases in v_C there is also a steady solution.

Two interesting observations can be made from figure 2. Firstly, it appears that the axial length of the interface does not change with the rotation rate. This is in contrast to many of the simulation results presented in Carrasco-Teja & Frigaard (2009), where buoyancy was not dominant, i.e. $|\tilde{b}| \sim O(1)$. Secondly, we observe that the orientation of the streamlines changes. In each simulation, the interfacial region

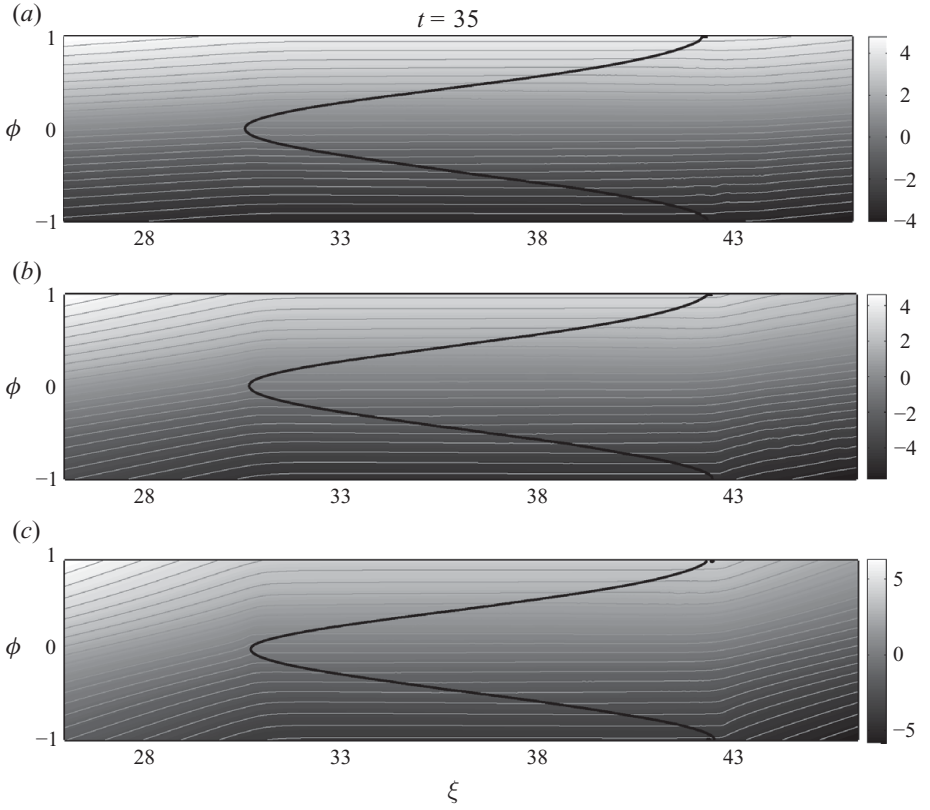

FIGURE 2. Streamlines and interface ($\bar{c}(\phi, \xi) = 0.5$) at $t = 35$ from the two-dimensional numerical simulation: (*a*) $v_C = 0.1$; (*b*) $v_C = 0.3$; (*c*) $v_C = 0.5$. Other model parameters are $\kappa_1 = 1$, $\kappa_2 = 0.25$, $e = 0.1$, $w_C = 0$, $\tilde{b} = -50$ ($\rho_1 = 1$, $\rho_2 = 0.9$, $St^* = 0.002$).

appears to be characterized by streamlines that are near-parallel to the annulus axis, but just outside this region the streamlines quickly become more angular. The angular behaviour is easily understood as it is simply associated with the Couette component from the rotation. We observe that the angle the streamlines make with the ξ-axis increases as the rotation rate is increased.

In figure 3 we present a second set of simulation results. This time we have a 1:4 viscosity ratio, small eccentricity again and have reduced $|\tilde{b}|$ slightly. For these parameters the fixed casing simulation is unsteady, as is captured in figure 3(*a*). We observe that the interface elongates progressively along the narrow side of the annulus, under the action of buoyancy. As the casing rotation rate is increased from zero, the displacement remains unsteady. In Carrasco-Teja & Frigaard (2009), for more modest $|\tilde{b}|$ we observed that $O(1)$ casing rotation could in fact stabilize an otherwise unsteady displacement, but for $|\tilde{b}| \gg 1$ this does not appear to occur. We also observe in figure 3(*d–f*) the same streamline behaviour as in figure 2.

3.2. *Derivation of the lubrication displacement model*

As we have seen, under conditions of dominant buoyancy and with modest casing motions, it is possible to have stable steady displacements with interfaces that become long. Assume that $\delta \ll 1$, $\delta(\hat{r_o} + \hat{r_i}/2) \ll 1$ and $c \sim \bar{c}$. We consider the case $|\tilde{b}| \gg 1$ and define $\epsilon = 1/|\tilde{b}| \ll 1$. As in Carrasco-Teja *et al.* (2008) we adopt the interface tracking

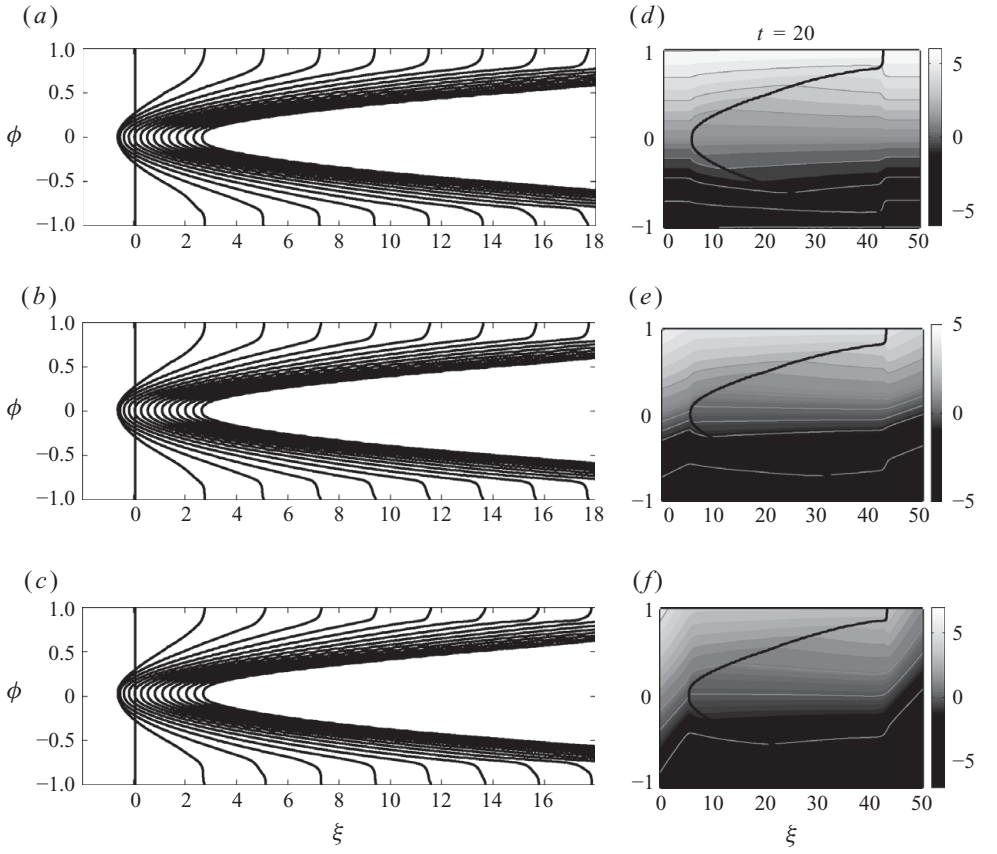

FIGURE 3. Examples of an unsteady displacement. (*a–c*) Interface ($\bar{c}(\phi,\xi)=0.5$) shown at $t=1, 2, 3\ldots15$. (*d–f*) Streamlines and interface shown at $t=20$: (*a* and *d*) $v_C=0$; (*b* and *e*) $v_C=0.1$; (*c* and *f*) $v_C=0.3$. Other model parameters are $\kappa_1=0.25, \kappa_2=1, e=0.1$, $w_C=0$, $\tilde{b}=-10$ ($\rho_1=1$, $\rho_2=0.9$, $St^*=0.01$).

formulation described in § 2.2. For simplicity we shall assume throughout that the displacing fluid 1 is heavier than the displaced fluid 2, and that the displacement front slumps towards the bottom of the annulus, $\phi=\pm1$. We also assume as in Carrasco-Teja *et al.* (2008) that the annulus is close to horizontal in the sense that $\cos\beta=\alpha\epsilon$ with $\alpha=O(1)$.

The main complication introduced by the casing rotation is that the closure relation between $\boldsymbol{S}_k$ and $\nabla\Psi$ in each fluid is not easily specified for non-zero (v_C, w_C). Thus, the way to reduce the equations further is not immediately apparent. One might consider working with either $\boldsymbol{S}_k$ or $\nabla\Psi$. Our choice of variable is dictated by the example results of figures 2 and 3, which have shown that long-thin interfaces are characterized by near-parallel streamlines within the interfacial region (but not outside in the single-phase regions). Thus, we assume the following scaling

$$\text{(i)}\left|\frac{\partial\Psi}{\partial\xi}\right|=O(\epsilon),\quad \text{(ii)}\left|\frac{\partial\Psi}{\partial\phi}\right|=O(1),\quad \text{(iii)}\left|\frac{\partial\phi_i}{\partial\xi}\right|=O(\epsilon). \tag{3.1}$$

From (2.22) we observe that (i) of (3.1) implies $|S_{k,\xi}|=O(v_C)+O(\epsilon)$, and (ii) of (3.1) implies $|S_{k,\phi}|=O(w_C)+O(1)$.

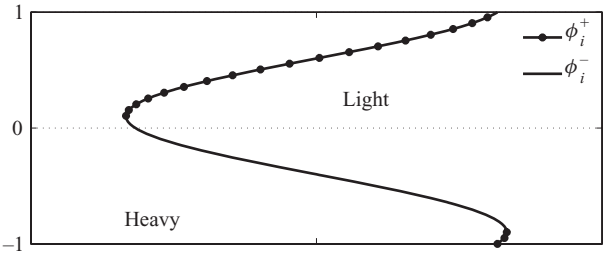

FIGURE 4. Schematic of the asymmetric interface.

We rescale axial distances and time as follows: $z=\epsilon\xi$, $\tilde{t}=\epsilon t$, $\bar{w}=W$, $\bar{v}=\epsilon V$. The interface position is now $\phi=\phi_i(z,\tilde{t})$ and the kinematic equation:

$$2H\frac{\partial\phi_i}{\partial\tilde{t}}+\frac{\partial\Psi}{\partial\phi}\frac{\partial\phi_i}{\partial z}+\frac{\partial\Psi}{\partial z}=0, \tag{3.2}$$

where $2HV=-\Psi_z$, $2HW=\Psi_\phi$.

The scales on $\boldsymbol{S}$ may be used to derive the pressure scaling:

$$-p_\xi-\frac{\rho_k\cos\beta}{St^*}=-\epsilon p_z-\alpha\frac{\rho_k}{|\rho_2-\rho_1|}=S_{k,\phi}=O(w_C)+O(1).$$

This suggests that we introduce $P=\epsilon p$ as a rescaled pressure, i.e.

$$S_{k,\phi}=-P_z-\alpha\frac{\rho_k}{|\rho_2-\rho_1|}.$$

Using (2.22) and the scaling of $S_{k,\xi}$ we have

$$\begin{aligned}\frac{1}{\epsilon}\left[P_\phi-\frac{\rho_k}{|\rho_2-\rho_1|}\sin\pi\phi+O(\epsilon^2)\right]&=p_\phi-\frac{\rho\sin\beta\sin\pi\phi}{St^*},\\&=S_{k,\xi}=v_C\frac{1}{2H^2}\left[\frac{m_1+m_0}{m_0m_2-m_1^2}\right]_k+O(\epsilon).\end{aligned} \tag{3.3}$$

We suppose that the interface has slumped towards the narrow side of the annulus, $\phi=\pm1$, due to buoyancy effects (see figure 4). At any fixed z, as we increase $\phi\in[-1,1]$ we will cross the interface exactly twice (thus our use of $\phi=\phi_i(z,\tilde{t})$ is not precise, as the function is double valued). We shall denote the two crossing positions by ϕ_i^- and ϕ_i^+, with $\partial\phi_i^-/\partial z>0$, $\partial\phi_i^+/\partial z<0$, and assume the narrow side is occupied by the heavier fluid 1. If instead the narrow side is occupied by light fluid, similar expressions hold.

We integrate (3.3) with respect to ϕ at fixed z, within the interfacial zone, giving the following expressions, valid to $O(\epsilon^2)$:

$$\begin{aligned}P(\phi,z,t)=P(-1,z,t)-\frac{\rho_1}{\pi|\rho_2-\rho_1|}[\cos\pi\phi+1]+\epsilon v_C\int_{-1}^{\phi}\frac{1}{2H^2}\left[\frac{m_1+m_0}{m_0m_2-m_1^2}\right]_1\mathrm{d}\phi,\\ \phi\in[-1,\phi_i^-],\end{aligned} \tag{3.4}$$

$$P(\phi,z,t) = P(-1,z,t) - \frac{\rho_1}{\pi|\rho_2-\rho_1|} - \frac{\cos\pi\phi_i^-}{\pi} - \frac{\rho_2}{\pi|\rho_2-\rho_1|}\cos\pi\phi + \epsilon v_C \int_{-1}^{\phi_i^-} \frac{1}{2H^2}\left[\frac{m_1+m_0}{m_0m_2-m_1^2}\right]_1 \mathrm{d}\phi + \epsilon v_C \int_{\phi_i^-}^{\phi} \frac{1}{2H^2}\left[\frac{m_1+m_0}{m_0m_2-m_1^2}\right]_2 \mathrm{d}\phi, \quad \phi\in[\phi_i^-,\phi_i^+], \tag{3.5}$$

$$P(\phi,z,t) = P(-1,z,t) - \frac{\rho_1}{\pi|\rho_2-\rho_1|}[\cos\pi\phi+1] + \frac{\cos\pi\phi_i^+ - \cos\pi\phi_i^-}{\pi} + \epsilon v_C \int_{-1}^{\phi_i^-} \frac{1}{2H^2}\left[\frac{m_1+m_0}{m_0m_2-m_1^2}\right]_1 \mathrm{d}\phi + \epsilon v_C \int_{\phi_i^-}^{\phi_i^+} \frac{1}{2H^2}\left[\frac{m_1+m_0}{m_0m_2-m_1^2}\right]_2 \mathrm{d}\phi + \epsilon v_C \int_{\phi_i^+}^{\phi} \frac{1}{2H^2}\left[\frac{m_1+m_0}{m_0m_2-m_1^2}\right]_1 \mathrm{d}\phi, \quad \phi\in[\phi_i^+,1]. \tag{3.6}$$

We now impose periodicity of the pressure, i.e. $P(-1,z,t)=P(1,z,t)$, which leads directly to the condition:

$$0 = \frac{\cos\pi\phi_i^+ - \cos\pi\phi_i^-}{\pi} + \epsilon v_C \int_{-1}^{\phi_i^-} \frac{1}{2H^2}\left[\frac{m_1+m_0}{m_0m_2-m_1^2}\right]_1 \mathrm{d}\phi + \epsilon v_C \int_{\phi_i^-}^{\phi_i^+} \frac{1}{2H^2}\left[\frac{m_1+m_0}{m_0m_2-m_1^2}\right]_2 \mathrm{d}\phi + \epsilon v_C \int_{\phi_i^+}^{1} \frac{1}{2H^2}\left[\frac{m_1+m_0}{m_0m_2-m_1^2}\right]_1 \mathrm{d}\phi. \tag{3.7}$$

Only the first term above is of order 1, and thus we have the leading-order condition that $\cos\pi\phi_i^+ = \cos\pi\phi_i^-$ which implies that $\phi_i^- = -\phi_i^+$. This has the important conclusion that at leading order the interface will be symmetric about wide and narrow sides of the annulus. We may readily see that in the above expression the effect of casing rotation comes in at first order on the 'symmetry' of the interface. This is not to say that casing rotation cannot affect the shape of the interface at leading order.

3.2.1. *Perturbation expansion*

Having determined the orders of magnitude of the various terms and some basic properties of the solution above, we now proceed in a formal perturbation expansion:

$$\begin{aligned}\Psi &\sim \Psi_0 + \epsilon\Psi_1 + \epsilon^2\Psi_2 + \ldots,\\ P &\sim P_0 + \epsilon P_1 + \epsilon^2 P_2 + \ldots,\\ \boldsymbol{S}_k &\sim \boldsymbol{S}_{k,0} + \epsilon\boldsymbol{S}_{k,1} + \epsilon^2\boldsymbol{S}_{k,2} + \ldots,\\ \phi_i^{\pm} &\sim \phi_{i,0}^{\pm} + \epsilon\phi_{i,1}^{\pm} + \epsilon^2\phi_{i,2}^{\pm} + \ldots.\end{aligned}$$

Above we have established that $\phi_{i,0}^- = -\phi_{i,0}^+$, and we shall simply write $\phi_{i,0}^+ = \phi_i$ for the leading-order symmetric interface. The leading-order pressure is given by the even function $P_0(-\phi,z,t) = P_0(\phi,z,t)$:

$$P_0(\phi,z,t) = \begin{cases} P(1,z,t) - \dfrac{\rho_1(1+\cos\pi\phi)}{\pi|\rho_2-\rho_1|} + \dfrac{\cos\pi\phi - \cos\pi\phi_i}{\pi}, & \phi\in[0,\phi_i],\\ P(1,z,t) - \dfrac{\rho_1(1+\cos\pi\phi)}{\pi|\rho_2-\rho_1|}, & \phi\in[\phi_i,1]. \end{cases} \tag{3.8}$$

The equations governing $\boldsymbol{S}_k$ are (2.23) and (2.24), which to leading order give

$$\frac{\partial S_{k,0,\phi}}{\partial \phi} = 0, \tag{3.9}$$

$$\frac{\partial S_{k,1,\phi}}{\partial \phi} = -\frac{\partial S_{k,0,z}}{\partial z}. \tag{3.10}$$

Thus, $S_{k,0,\phi}$ is independent of ϕ in each layer and using the leading-order pressure:

$$S_{1,\phi} = -P_z(1,z,t) - \alpha\frac{\rho_1}{|\rho_2-\rho_1|}, \tag{3.11}$$

$$S_{2,\phi} = -P_z(1,z,t) - \alpha\frac{\rho_2}{|\rho_2-\rho_1|} - \sin\pi\phi_i\frac{\partial \phi_i}{\partial z},$$

$$S_{2,\phi} = S_{1,\phi} + \alpha - \sin\pi\phi_i\frac{\partial \phi_i}{\partial z}. \tag{3.12}$$

To proceed further we need to fix the closure relation between $\boldsymbol{S}_k$ and $\nabla\Psi$. As discussed in § 2.1.1 and described in detail in the Appendix, the closure relations may be formulated and computed in many different ways. For the lubrication model, the most convenient is to specify both Ψ_ξ and S_ϕ, and compute Ψ_ϕ and S_ξ. Therefore, we assume the following relationships hold:

$$\Psi_\phi = F_{k,1}(S_{k,\phi}, \Psi_\xi), \tag{3.13}$$

$$S_{k,\xi} = F_{k,2}(S_{k,\phi}, \Psi_\xi), \tag{3.14}$$

where $F_{k,1}$ and $F_{k,2}$ are sufficiently smooth for what follows. Note that $\Psi_\xi \sim \epsilon\Psi_{0,z} + O(\epsilon^2)$, and thus via a Taylor expansion we have

$$\Psi_{0,\phi} = F_{k,1}(S_{k,0,\phi}, 0), \tag{3.15}$$

$$S_{k,0,z} = F_{k,2}(S_{k,0,\phi}, 0), \tag{3.16}$$

$$\Psi_{1,\phi} = S_{k,1,\phi}\frac{\partial F_{k,1}}{\partial S_{k,\phi}}(S_{k,0,\phi}, 0) + \Psi_{0,z}\frac{\partial F_{k,1}}{\partial \Psi_\xi}(S_{k,0,\phi}, 0). \tag{3.17}$$

As in Pelipenko & Frigaard (2004*c*) and Carrasco-Teja *et al.* (2008), the leading-order stream function and pressure gradient are now determined via consideration of the global mass conservation, i.e. the periodic boundary condition on Ψ

$$4 = \Psi(1,z,\tilde{t}) - \Psi(-1,z,\tilde{t}) = \int_{-1}^{1}\Psi_\phi\,\mathrm{d}\phi. \tag{3.18}$$

On expanding (3.18) with respect to ϵ, and exploiting the symmetry of the leading-order interface, the zeroth-order expression is

$$2 = \int_0^1 \Psi_{0,\phi}\,\mathrm{d}\phi = \int_0^{\phi_i} F_{2,1}(S_{2,0,\phi}, 0)\,\mathrm{d}\phi + \int_{\phi_i}^1 F_{1,1}(S_{1,0,\phi}, 0)\,\mathrm{d}\phi,$$

$$= \int_0^{\phi_i} F_{2,1}(A, 0)\,\mathrm{d}\phi + \int_{\phi_i}^1 F_{1,1}(A-b, 0)\,\mathrm{d}\phi, \tag{3.19}$$

$$b = \alpha - \sin\pi\phi_i\frac{\partial \phi_i}{\partial z}, \quad A = S_{2,0,\phi}. \tag{3.20}$$

We note that the functions $F_{k,1}(S_{k,\phi}, \Psi_\xi)$ increase strictly monotonically with respect to the first argument and thus A is uniquely determined at each z. Furthermore, we may observe that the dependency on $(z,\tilde{t})$ enters only via ϕ_i and $\partial\phi_i/\partial z$.

For a given symmetric leading-order interface, $\phi_i(z,\tilde{t})$, let us assume that we have computed $A(z,\tilde{t})$ from (3.19) at each z. Thus, we have $S_{k,0,\phi}$ determined in each fluid and also Ψ_0, via integration, e.g.

$$\Psi_0 = \int_0^{\phi} F_{2,1}(S_{2,0,\phi}, 0)\,\mathrm{d}\phi, \quad \phi \in [0, \phi_i].$$

Therefore $\Psi_0 = \Psi_0(\phi, \phi_i(z,\tilde{t}), \partial\phi_i/\partial z(z,\tilde{t}))$. From symmetry considerations, we may infer that Ψ_0 is an odd function of ϕ. Using (3.16) we may also compute $S_{k,0,z}$.

Defining $\Phi_i(\phi_i) = \int_0^{\phi_i} H\,\mathrm{d}\phi$, as the volumetric position of the leading-order interface, the leading-order kinematic equation is

$$\frac{\partial \Phi_i}{\partial \tilde{t}} + \frac{\partial q}{\partial z}\left(\Phi_i, \Phi_{i,z}\right) = 0, \tag{3.21}$$

where

$$q\left(\Phi_i(z,\tilde{t}), \Phi_{i,z}(z,\tilde{t})\right) = \frac{1}{2}\Psi_0\left(\phi = \phi_i(z,\tilde{t}), \phi_i(z,\tilde{t}), \frac{\partial \phi_i}{\partial z}(z,\tilde{t})\right).$$

This completes the leading-order solution.

3.2.2. *First-order perturbation*

To understand the asymmetry induced by casing rotation, we need to consider the first-order perturbation. To start with, we may consider the first-order terms in (3.18), which are found to be

$$\begin{aligned} 0 = \phi_{i,1}^{-}\left[\Psi_{0,\phi}\left(\phi_{i,0}^{-,-}\right) - \Psi_{0,\phi}\left(\phi_{i,0}^{-,+}\right)\right] - \phi_{i,1}^{+}\left[\Psi_{0,\phi}\left(\phi_{i,0}^{+,+}\right) - \Psi_{0,\phi}\left(\phi_{i,0}^{-,-}\right)\right] \\ + \int_{-1}^{\phi_{i,0}^{-}} \Psi_{1,\phi}\,\mathrm{d}\phi + \int_{\phi_{i,0}^{-}}^{\phi_{i,0}^{+}} \Psi_{1,\phi}\,\mathrm{d}\phi + \int_{\phi_{i,0}^{+}}^{1} \Psi_{1,\phi}\,\mathrm{d}\phi, \end{aligned} \tag{3.22}$$

where $\phi_{i,0}^{-,-}$ is the limit as $\phi_{i,0}^{-}$ approached from below, etc. Using the fact that $\Psi_{0,\phi}$ is an even function and substituting from (3.17) we have

$$\begin{aligned} 0 = &\left[\phi_{i,1}^{-} - \phi_{i,1}^{+}\right]\left[\Psi_{0,\phi}\left(\phi_{i,0}^{+,+}\right) - \Psi_{0,\phi}\left(\phi_{i,0}^{-,-}\right)\right] \\ &+ \int_{-1}^{\phi_{i,0}^{-}} S_{1,1,\phi}\frac{\partial F_{1,1}}{\partial S_{1,\phi}}(S_{1,0,\phi}, 0) + \Psi_{0,z}\frac{\partial F_{1,1}}{\partial \Psi_{\xi}}(S_{1,0,\phi}, 0)\,\mathrm{d}\phi \\ &+ \int_{\phi_{i,0}^{-}}^{\phi_{i,0}^{+}} S_{2,1,\phi}\frac{\partial F_{2,1}}{\partial S_{2,\phi}}(S_{2,0,\phi}, 0) + \Psi_{0,z}\frac{\partial F_{2,1}}{\partial \Psi_{\xi}}(S_{2,0,\phi}, 0)\,\mathrm{d}\phi \\ &+ \int_{\phi_{i,0}^{+}}^{1} S_{1,1,\phi}\frac{\partial F_{1,1}}{\partial S_{1,\phi}}(S_{1,0,\phi}, 0) + \Psi_{0,z}\frac{\partial F_{1,1}}{\partial \Psi_{\xi}}(S_{1,0,\phi}, 0)\,\mathrm{d}\phi. \end{aligned} \tag{3.23}$$

We may observe that $S_{k,0,\phi}$ is an even function of ϕ and the partial derivatives of $F_{k,1}$ featured above are also even. From (3.10) we see that $S_{k,1,\phi}$ is an odd function of ϕ and equally we have that $\Psi_{0,z}$ is an odd function of ϕ. Combining this we find that all the integrals above vanish, leaving us with

$$\left[\phi_{i,1}^{+} - \phi_{i,1}^{-}\right]\left[\Psi_{0,\phi}\left(\phi_{i,0}^{+,+}\right) - \Psi_{0,\phi}\left(\phi_{i,0}^{-,-}\right)\right] = 0. \tag{3.24}$$

Note that $[\Psi_{0,\phi}(\phi_{i,0}^{+,+}) - \Psi_{0,\phi}(\phi_{i,0}^{-,-})]$ is proportional to the jump in tangential velocities across the interface, which will in general be non-zero due to different fluid rheological properties. Therefore, we have that

$$\phi_{i,1}^{+} = \phi_{i,1}^{-}. \tag{3.25}$$

Thus, the first-order perturbation of the interface gives the asymmetry due to rotation. To quantify the degree of asymmetry, we enforce the condition of periodicity of the pressure with respect to ϕ, i.e. we expand (3.7) to first order in ϵ, using (3.25) and the fact that the mobility moments m_j and leading-order interface are even:

$$\phi_{i,1}^{+}\sin\pi\phi_i = v_C\left[\int_0^{\phi_i}\frac{1}{2H^2}\left[\frac{m_1+m_0}{m_0m_2-m_1^2}\right]_2 \mathrm{d}\phi + \int_{\phi_i}^{1}\frac{1}{2H^2}\left[\frac{m_1+m_0}{m_0m_2-m_1^2}\right]_1 \mathrm{d}\phi\right]. \quad (3.26)$$

Since the integrand is positive definite, we see that the symmetric interface is perturbed by $O(\epsilon)$ in the direction of v_C, as above.

Note that typically we would not compute the moments m_j as part of the solution procedure, so the above is given for qualitative understanding. In developing the zeroth-order solution, we will have evaluated the leading-order $S_{k,0,z}$ from (3.16). This can be used to compute $\phi_{i,1}^{+} = \phi_{i,1}^{-}$:

$$\phi_{i,1}^{+}\sin\pi\phi_i = \int_0^{\phi_i} S_{2,0,z}\,\mathrm{d}\phi + \int_{\phi_i}^{1} S_{1,0,z}\,\mathrm{d}\phi. \quad (3.27)$$

Although we may proceed further to construct the first-order stream function perturbation and remainder of the first-order solution, our principal interest lies with behaviour of the leading-order interface and prediction of the asymmetry above.

3.3. *Computational verification and comments*

Figure 5 shows two comparisons between numerical solutions of the full two-dimensional problem, for Newtonian fluids, and the lubrication model. We have presented both the leading-order symmetric profile and the first-order asymmetric correction superimposed. The agreement is evidently good, and the asymmetric shift is verified to be small, i.e. $O(1/|\tilde{b}|)$, as expected.

An interesting feature of the flows we have modelled is the transition from the interfacial regime to the pure fluid regimes away from the interface. In the pure fluid regimes, the stream function adopts a solution in which $S_\xi = 0$, so that the azimuthal velocity matches the Couette shear component. It can be verified that in a pure fluid, $\nabla \cdot \boldsymbol{f} = 0$, so that the field equations for the stream function are satisfied when S_ϕ is independent of ϕ; S_ϕ is found iteratively by increasing S_ϕ until (3.18) is satisfied. It is interesting to note that, for example, if the two fluids were both Newtonian or were both power law, but with the same power law index, then the stream function far upstream and downstream of the interfacial would be identical to within a constant! Nevertheless, the streamlines are distorted in the interfacial region.

We should observe that some kind of matching region is necessary between the interfacial and far-field regions. In terms of our perturbation method, there is a transition layer between $\Psi_\xi \sim \epsilon$ in the interfacial region to $S_\xi \sim \epsilon$ in the pure fluid regions. The classical lubrication assumptions on the interface being long and thin, i.e. (iii) of (3.1), break down in the vicinity of the leading and trailing edge. For example, the expression (3.27) for the azimuthal shift in interface position becomes apparently singular at $\phi_i = 0,\ 1$. This is a characteristic of the breakdown of a regular perturbation procedure. We have not looked at the matching problem, although it is probably tractable. The same type of breakdown of the modelling assumptions occurs in most lubrication-style displacement (or thin film spreading) models.

Finally, note that since the first-order asymmetric shift is dependent only on the zeroth-order solution, via (3.27), one could use the lubrication model as a relatively quick simulation model for the full process, i.e. solving (3.21). The leading-order

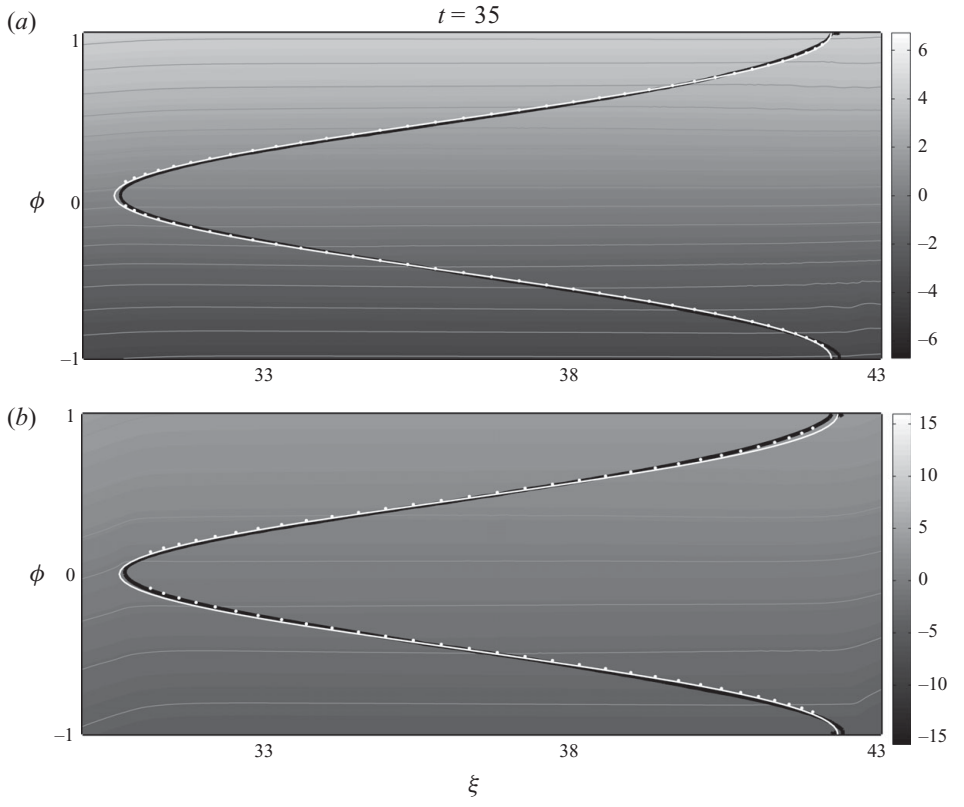

FIGURE 5. Comparison between the two-dimensional numerical solution (interface is the contour $\bar{c}(\phi, \xi) = 0.5$, in black), and the lubrication displacement model interface (leading-order symmetric solution in solid white; first-order asymmetric shift – white dots): (*a*) $v_C = 0.1$; (*b*) $v_C = 0.5$. Other model parameters are $\kappa_1 = 1, \kappa_2 = 0.25, e = 0.1, w_C = 0, \tilde{b} = -50$ ($\rho_1 = 1, \rho_2 = 0.9, St^* = 0.002$).

model is symmetric and it can be verified that (3.21) approaches the fixed casing limit (see (4.13) in Carrasco-Teja *et al.* 2008), as the casing speeds approach zero. Also the first-order asymmetry vanishes, since $S_{k,0,z} \to 0$ as $v_C \to 0$. We have not followed this computational route, but instead below we analyse (3.21) directly in order to ascertain if there exist steady travelling wave solutions.

4. Steady travelling wave solutions

As in Carrasco-Teja *et al.* (2008) the key feature that we wish to predict is whether or not steady travelling wave solutions exist, and to characterize the effects of casing motion. In computing the flux function, note that formally we have:

$$q\left(\Phi_i(z,\tilde{t}), \Phi_{i,z}(z,\tilde{t})\right) = q\left(\Phi_i(z,\tilde{t}), b\right): \quad b = \alpha - \sin\pi\phi_i \frac{\partial \phi_i}{\partial z}, \quad \Phi_i(\phi_i) = \int_0^{\phi_i} H \, \mathrm{d}\phi,$$

and note that the only difference in leading-order model between here and Carrasco-Teja *et al.* (2008) is in the detail of computing the closures. In particular we find that q increases monotonically with respect to b, and consequently (3.21) can be written

as:

$$\frac{\partial \Phi_i}{\partial \tilde{t}} + \frac{\partial q}{\partial \Phi_i}(\Phi_i, b)\frac{\partial \Phi_i}{\partial z} = \frac{\partial q}{\partial b}(\Phi_i, b)\frac{\partial}{\partial z}\left[\sin \pi\phi_i \frac{\partial \phi_i}{\partial z}\right], \tag{4.1}$$

from which we see that the coefficient multiplying $\Phi_{i,zz}$ will be positive. Therefore (3.21) is a quasi-linear advection–diffusion equation. We expect spreading of the interface relative to some advective motion of mean speed 1 (due to scaling considerations).

We seek a steady travelling wave solution, shifting to a moving frame, moving at a unit speed, $x = z - t$. We assume that the steady profile will be monotone and symmetric. Thus $\Phi_i(x)$ (or equivalently $x(\Phi_i)$), will satisfy

$$\left.\begin{array}{ll} x'(0) = 0, & x''(0) > 0, \\ x'(1) = 0, & x''(1) < 0, \\ x'(\Phi_i) > 0, & \Phi_i \in (0, 1). \end{array}\right\} \tag{4.2}$$

The function $\Phi_i(x)$ must satisfy the following equation:

$$q\left(\Phi_i, b(\Phi_i, \Phi_i')\right) - \Phi_i = 0, \tag{4.3}$$

which may also be interpreted as an algebraic equation for $x(\Phi_i)$. Furthermore, by exactly the same methods as in Carrasco-Teja *et al.* (2008), we may prove the following.

THEOREM 1. *The condition that*

$$q(\Phi_i, \alpha) \geqslant \Phi_i \quad \textit{for all} \quad \Phi_i \in [0, 1] \tag{4.4}$$

is a necessary and sufficient condition for the existence of a steady-state travelling wave solution to (3.21), that also satisfies the conditions (4.2).

4.1. *Newtonian fluids*

Newtonian fluids form an important special case. We may note that all mobility moments m_j are constant: $m_j = 1/(j\kappa_k)$ in fluid k. This means that the leading-order solution may be calculated semi-implicitly. The flux function $q(\Phi_i, b)$ is given by

$$q(\Phi_i, b) = \frac{I_L}{\frac{\kappa_2}{\kappa_1} I_H + I_L} + \frac{w_C}{2}\left[\Phi_i - \frac{I_L}{\frac{\kappa_2}{\kappa_1} I_H + I_L}\right] + \frac{\frac{\kappa_2}{\kappa_1} I_L}{\frac{b}{3\kappa_1} I_H + I_L}, \tag{4.5}$$

where

$$I_L = \int_0^{\phi_i} H(\phi)^3 \, \mathrm{d}\phi, \quad I_H = \int_{\phi_i}^1 H(\phi)^3 \, \mathrm{d}\phi.$$

The condition to have a steady state for two Newtonian fluids is therefore given by

$$\kappa_1/\kappa_2 > \frac{\Phi_i I_H}{(1-\Phi_i) I_L} - \frac{\alpha I_H}{3\left(1 - \frac{w_C}{2}\right)(1-\Phi_i)\kappa_2}, \qquad \forall \Phi_i \in [01]. \tag{4.6}$$

Note that for a completely horizontal well $\alpha = 0$, the axial velocity does not affect this ratio. Apart from the w_C term, this expression is identical with that for the stationary casing flows in Carrasco-Teja *et al.* (2008). We may straightforwardly compute the critical viscosity ratio necessary to satisfy the condition (4.4) at different w_C and α/κ_2. It is interesting that only the axial casing velocity affects the leading-order solution. Casing rotation v_C introduces a first-order asymmetry of the interface,

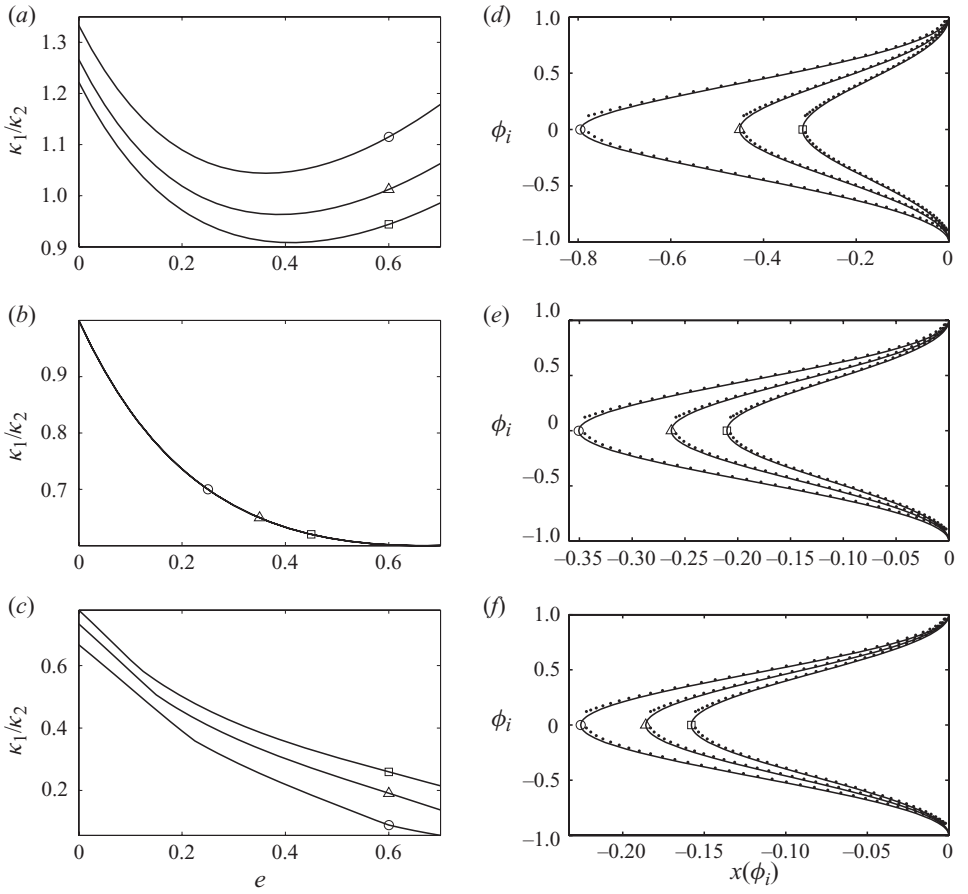

FIGURE 6. Effects of small inclination from horizontal on steady-state displacement solutions for two Newtonian fluids: (*a–c*) critical viscosity ratio above which we have a steady-state displacement solution; (*d–f*) sample steady-state shapes (solid lines) and with first-order asymmetric corrections (dotted lines) (parameters are $\kappa_1/\kappa_2 = 1.5$, $e = 0.1$); (*a* and *d*) $\alpha = -1$; (*b* and *e*) $\alpha = 0$; (*c* and *f*) $\alpha = 1$. In each figure we plot $w_C = -0.5$ (□), 0 (△), 0.5 (○). Other model parameters are $v_C = 0.5, \tilde{b} = -50$.

i.e. the interface positions are at

$$\phi = -\phi_i + \epsilon\phi_{i,1}^-, \quad \phi = \phi_i + \epsilon\phi_{i,1}^+, \quad \phi_{i,1}^+ = \phi_{i,1}^-,$$

where

$$\phi_{i,1}^+ \sin \pi\phi_i = \frac{3v_C}{2}\left[\kappa_2 \int_0^{\phi_i} \frac{1}{H^2}\,\mathrm{d}\phi + \kappa_1 \int_{\phi_i}^1 \frac{1}{H^2}\,\mathrm{d}\phi\right]. \tag{4.7}$$

This explains the apparently identical axial extensions of the interfaces shown earlier in figure 2, computed from the two-dimensional model.

In figure 6(*a–c*) we explore the variation in critical viscosity ratio with the annular eccentricity, for different inclination parameters α (recall that $\alpha < 1$ means that the heavy fluid is displacing the lighter fluid downhill). When displacing downhill (figure 6*a*), a positive axial casing velocity requires a larger viscosity ratio to achieve a steady displacement than does a negative axial casing velocity. When displacing uphill (figure 6*c*), this trend is reversed. For a perfectly horizontal annulus there is no effect of the casing motion. We observe a decrease in viscosity ratio for increasing

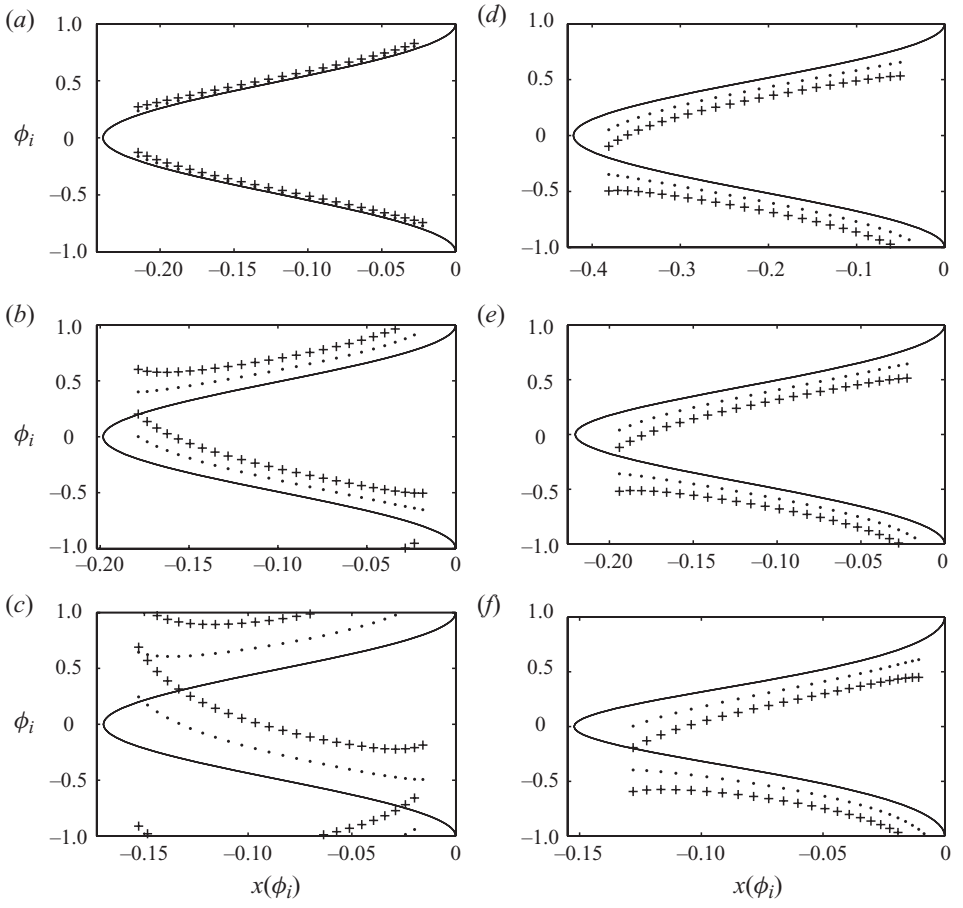

FIGURE 7. Steady-state shapes for two Newtonian fluids with varying casing rotating speeds. (*a*) $\kappa_1/\kappa_2 = 1.5$; (*b*) $\kappa_1/\kappa_2 = 1.7$; (*c*) $\kappa_1/\kappa_2 = 1.9$. For each plot $e = 0.05$, and interfaces are plotted at $v_C = 0$ (−), $1(\cdots)$, 2 (+) . (*d*) $e = 0$; (*e*) $e = 0.2$; (*f*) $e = 0.4$. For each plot $\kappa_1/\kappa_2 = 1.2$, and interfaces are plotted at $v_C = 0$ (−), $-1(\cdots)$, -2 (+). Other model parameters are $w_C = 0.3$, $\tilde{b} = -20$.

eccentricity, which parallels the fixed casing results in Carrasco-Teja *et al.* (2008). Physically, buoyancy causes the interface to slump towards the bottom of the annulus, which is a destabilizing effect. A small amount of eccentricity counters the slumping, by making it harder to flow on the narrow side. At large enough eccentricities the critical viscosity ratio increases, as it becomes increasingly difficult to flow on the narrow side, and we therefore see a minimum in the viscosity ratio needed for a steady-state displacement (e.g. see figure 6*a*).

Figure 6(*d–f*) shows examples of the steady-state shapes, at small eccentricity, $e = 0.1$, and with $\kappa_1/\kappa_2 = 1.5$. A positive axial velocity tends to elongate the steady-state profile as does a downhill displacement. The asymmetric first-order perturbation is shown with the dotted profile, but only in the central part of the interfacial region since we have seen that the perturbation procedure breaks down at the ends of this region.

Figure 7 shows the effects of increasing casing rotation rates: both positive and negative. The basic effect is of course to accentuate the asymmetry in the leading order. As we increase the viscosity ratio, steady-state shapes become shorter (see

figure 7*a–c*). Moderate increases in eccentricity also result in a shorter steady state (see figure 7*d–f*).

4.2. *Power law fluids*

For power law fluids, we are unable to compute directly the flux function $q(\Phi_i, b)$, as the closure relation is not specified algebraically. However, we may demonstrate that the conditions under which a steady-state exists can be expressed in terms of a consistency ratio. To see this, consider first the closure problem for a power law fluid. We have (see also Appendix):

$$\frac{\partial}{\partial y}\boldsymbol{\tau} = -\boldsymbol{G}, \quad \boldsymbol{\tau} = (\tau_{\phi y}, \tau_{\xi y}) = \kappa \dot{\gamma}^{n-1} \frac{\mathrm{d}}{\mathrm{d}y}\boldsymbol{u}.$$

The boundary conditions for $\boldsymbol{u} = (v, w)$ are $\boldsymbol{u} = \boldsymbol{u}_C$ at $y = -H$ and $\boldsymbol{u} = 0$ at $y = H$. On dividing through by κ we observe that the local velocity $\boldsymbol{u}$ depends only on n, H, $\boldsymbol{u}_C$ and $\boldsymbol{G}/\kappa = (G_\phi/\kappa, G_\xi/\kappa)$. Therefore, the closure expression (3.13), we may observe that

$$F_{k,1}(S_{k,\phi}, 0) = F_{k,1}(S_{k,\phi}/\kappa_k; n_k, H, \boldsymbol{u}_C),$$

and we know that $F_{k,1}$ increases monotonically with its first argument.

Suppose now at any Φ_i we define A_L/κ_2 and A_H/κ_1 by

$$\Phi_i = \frac{1}{2}\int_0^{\phi_i} F_{L,1}(A_L/\kappa_2; n_2, H, \boldsymbol{u}_C)\,\mathrm{d}\phi, \quad 1 - \Phi_i = \frac{1}{2}\int_{\phi_i}^{1} F_{H,1}(A_H/\kappa_1; n_1, H, \boldsymbol{u}_C)\,\mathrm{d}\phi. \tag{4.8}$$

Following the procedure in Carrasco-Teja *et al.* (2008), these integrals increase monotonically with respect to A_k/κ_k, and hence for fixed Φ_i, n_k, e and $\boldsymbol{u}_C$ we may compute both A_k/κ_k iteratively. We may therefore write

$$A_L/\kappa_2 = f_L(\Phi_i, n_2, e, \boldsymbol{u}_C); \quad A_H/\kappa_1 = f_H(1 - \Phi_i, n_1, e, \boldsymbol{u}_C). \tag{4.9}$$

We now define $b(\Phi_i) = A_L - A_H = f_L(\Phi_i, n_2, e, \boldsymbol{u}_C)\kappa_2 - f_H(1-\Phi_i, n_1, e, \boldsymbol{u}_C)\kappa_1$. Also we have that $b = \alpha - \sin\pi\phi_i(\partial\phi_i^+/\partial z)$ along the steady state, and require that $(\partial\phi_i^+/\partial z) > 0$ for $\phi_i \in [0, 1]$. This gives us the condition

$$\kappa_1/\kappa_2 > \frac{f_L(\Phi_i, n_2, e, \boldsymbol{u}_C) - \alpha/\kappa_2}{f_H(1 - \Phi_i, n_1, e, \boldsymbol{u}_C)}, \quad \forall \Phi_i \in [0, 1], \tag{4.10}$$

in order for there to be a steady travelling wave displacement; compare with (4.26) in Carrasco-Teja *et al.* (2008).

Figure 8 explores variations in the critical consistency ratio, κ_1/κ_2, in a horizontal annulus with no axial motion of the inner cylinder. We explore the effects of varying n_1 and n_2 at small $e = 0.2$, for different v_C. Note here that the casing rotation rate does enter into the conditions for there to be a steady state, unlike the Newtonian fluid case. We observe that the critical consistency ratio decreases with n_1 and increases with n_2. These effects are expected on physical grounds as they simply correspond to the displacing fluid becoming more (or less) viscous than the displaced fluid. More surprising is the relative insensitivity of the critical consistency ratio to the casing rotation rate.

The shear-thinning effects of casing rotation manifest more in the shape of the interface, as shown in figure 8(*c*, *d*). For identical power law indices (figure 8*a*), as the rotation rate increases the effective viscosity drops and it appears that the interface elongates. In figure 8(*b*) the power law index of the displacing fluid is larger than that of the displaced fluid. As the rotation rate increases the effective

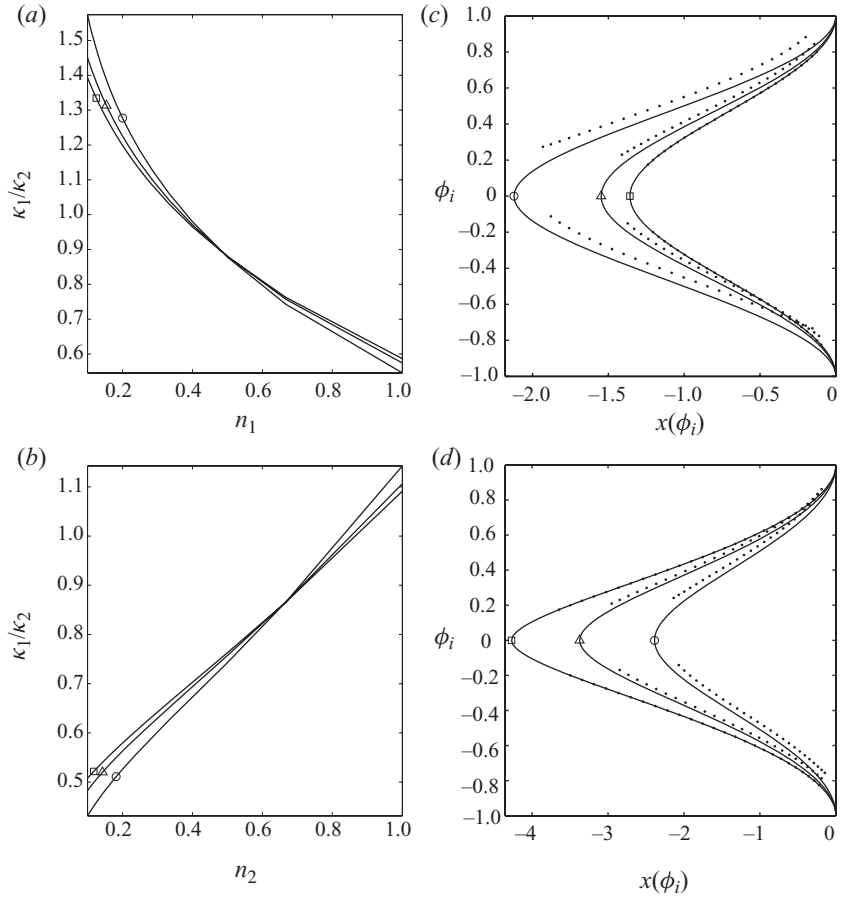

FIGURE 8. (a, b) Effects of power law indices on the critical consistency ratio necessary to have a steady state for two power law fluids: (a) $n_2 = 0.2$, variations with n_1; (b) $n_1 = 0.66$, variations with n_2. Other model parameters: $w_C = 0$, $\alpha = 0$, $e = 0.2$, and we plot $v_C = 0$ (□), 0.5 (△), 1 (○). (c, d) Sample steady-state shapes (solid lines) and asymmetric shifts (dotted lines) for $\tilde{b} = -20$: (c) $\kappa_1/\kappa_2 = 1.45$, $n_1 = 0.2$, $n_2 = 0.2$; (d) $\kappa_1/\kappa_2 = 0.6$, $n_1 = 0.66$, $n_2 = 0.2$.

viscosity of the displaced fluid decreases more rapidly than that of the displacing fluid. The consequence is that the interface shortens with rotation rate, which is perhaps counterintuitive.

Figure 9 explores the effects of axial casing velocity for two power law fluids. In figure 9(a, b) we explore variations in the critical consistency ratio, κ_1/κ_2, with power law indices. The results are qualitatively similar to figure 8 in that increasing n_1 decreases the critical consistency ratio, whereas increasing n_2 increases the critical consistency ratio. The effects of reciprocation w_C do however appear to be more pronounced than those of changing v_C. It also appears that when $n_1 > n_2$ a positive w_C reduces the critical κ_1/κ_2, but for $n_1 < n_2$ this effect is reversed. The crossover is however approximately at $n_1 = n_2$. In figure 9(c, d) we observe that the interface length elongates with w_C.

4.3. *Bingham fluids*

For any yield stress fluids, we can follow the procedure of the above section, to at least determine the functional dependency of the conditions for there to be steady-state

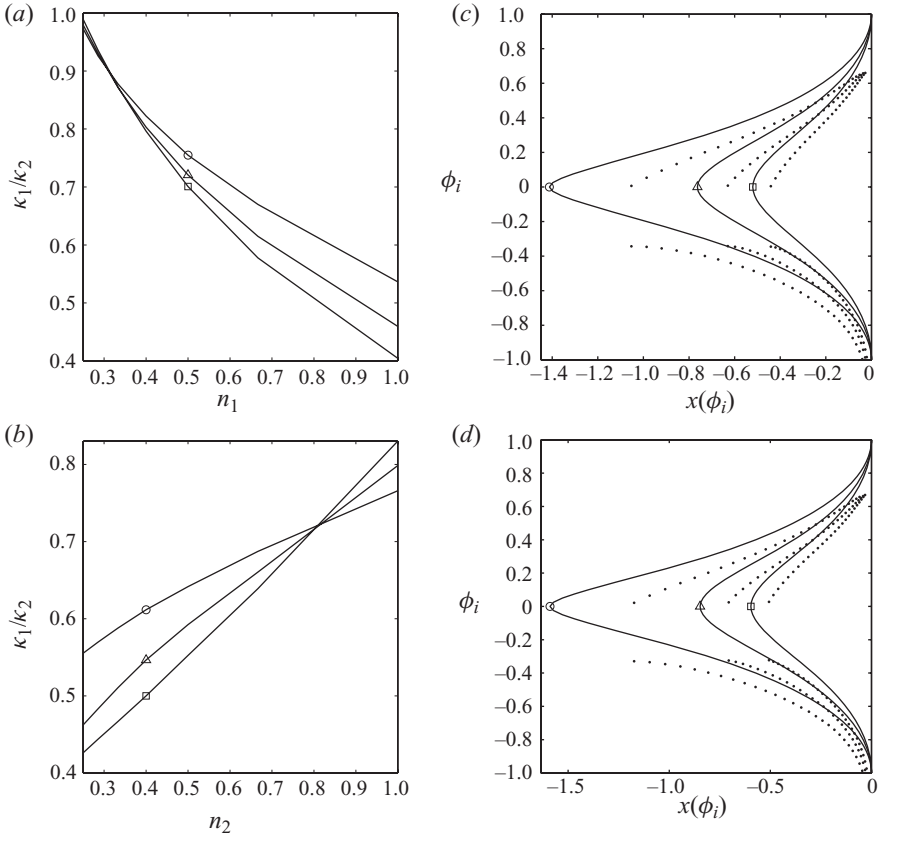

FIGURE 9. (*a*, *b*) Effects of power law indices on the critical consistency ratio necessary to have a steady state for two power law fluids: (*a*) $n_2 = 0.4$, variations with n_1; (*b*) $n_1 = 0.8$, variations with n_2. Other model parameters: $v_C = -1$, $\alpha = 0$, $e = 0.3$, and we plot $w_C = 0$ (□), 0.5 (△), 1 (○). (*c*, *d*) Sample steady-state shapes (solid lines) and asymmetric shifts (dotted lines) for $\tilde{b} = -10$ and $\kappa_1/\kappa_2 = 0.6$: (*c*) $n_1 = 0.9$, $n_2 = 0.4$; (*d*) $n_1 = 0.8$, $n_2 = 0.3$.

solutions. The closure expression (3.13) is

$$F_{k,1}(S_{k,\phi}, 0) = F_{k,1}(S_{k,\phi}/\kappa_k; B_k, n_k, H, \boldsymbol{u}_C),$$

with $B_k = \tau_{k,Y}/\kappa_k$. We define A_L/κ_2 and A_H/κ_1 by

$$\Phi_i = \frac{1}{2}\int_0^{\phi_i} F_{L,1}(A_L/\kappa_2; B_2, n_2, H, \boldsymbol{u}_C)\,\mathrm{d}\phi,$$

$$1 - \Phi_i = \frac{1}{2}\int_{\phi_i}^1 F_{H,1}(A_H/\kappa_1; B_1, n_1, H, \boldsymbol{u}_C)\,\mathrm{d}\phi.$$

Again these integrals increase monotonically with respect to A_k/κ_k, and therefore may be inverted:

$$A_L/\kappa_2 = f_L(\Phi_i, B_2, n_2, e, \boldsymbol{u}_C), \quad A_H/\kappa_1 = f_H(1 - \Phi_i, B_1, n_1, e, \boldsymbol{u}_C), \tag{4.11}$$

resulting again in the condition

$$\kappa_1/\kappa_2 > \frac{f_L(\Phi_i, B_2, n_2, e, \boldsymbol{u}_C) - \alpha/\kappa_2}{f_H(1 - \Phi_i, B_1, n_1, e, \boldsymbol{u}_C)}, \quad \forall \Phi_i \in [0, 1], \tag{4.12}$$

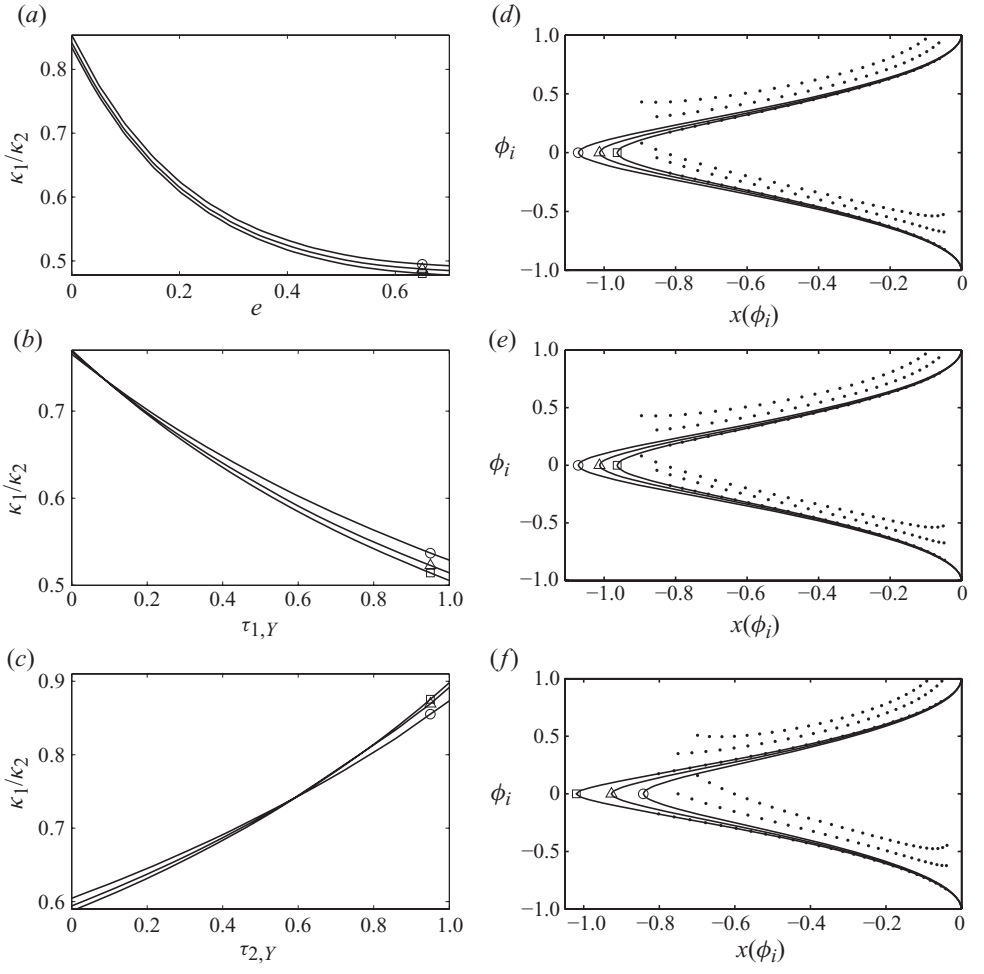

FIGURE 10. (a–c) Critical consistency ratio above which we have a steady-state displacement solution: (a) κ_1/κ_2 versus e, with $\tau_{1,Y}=0.2, \tau_{2,Y}=0.1$; ($b$) κ_1/κ_2 versus $\tau_{1,Y}$ with $e=0.2$, $\tau_{2,Y}=0.1$; (c) κ_1/κ_2 versus $\tau_{2,Y}$ with $e=0.2$, $\tau_{1,Y}=0.5$. Other model parameters are $w_C=0, \alpha=0$, and in each figure we plot $v_C=0$ (□), 0.5 (△), 1 (○). (d–f) Sample steady-state shapes (solid lines) and with first-order asymmetric corrections (dotted lines): (d) $\kappa_1/\kappa_2=0.72, \tau_{1,Y}=0.2, \tau_{2,Y}=0.1$; ($e$) $\kappa_1/\kappa_2=0.75, \tau_{1,Y}=0.2, \tau_{2,Y}=0.1$; ($f$) $\kappa_1/\kappa_2=0.9, \tau_{1,Y}=0.5, \tau_{2,Y}=0.9$. In each figure we plot $v_C=-0.5$ (□), 0 (△), 0.5 (○). Other model parameters are $e=0.2$, $\tilde{b}=-20$.

in order for there to be a steady travelling wave displacement. For Bingham fluids in particular, we set $n_1=n_2=1$.

Figure 10 shows typical variations in critical consistency ratio for two Bingham fluids, as the eccentricity or either of the yield stresses is increased. The variation with e is qualitatively as before, with Newtonian fluids, and the qualitative effects of changing the yield stress of either fluid are predictable in terms of their effect on the fluid viscosity, i.e. increasing the yield stress also increases the effective viscosity. Hence increasing $\tau_{1,Y}$ reduces the critical κ_1/κ_2 and increasing $\tau_{2,Y}$ increases the critical κ_1/κ_2. As before we observe that the critical conditions are not affected much by changes in v_C. Figure 10(d–e) shows example steady-state profiles. In figures 10(a) and 10(b)

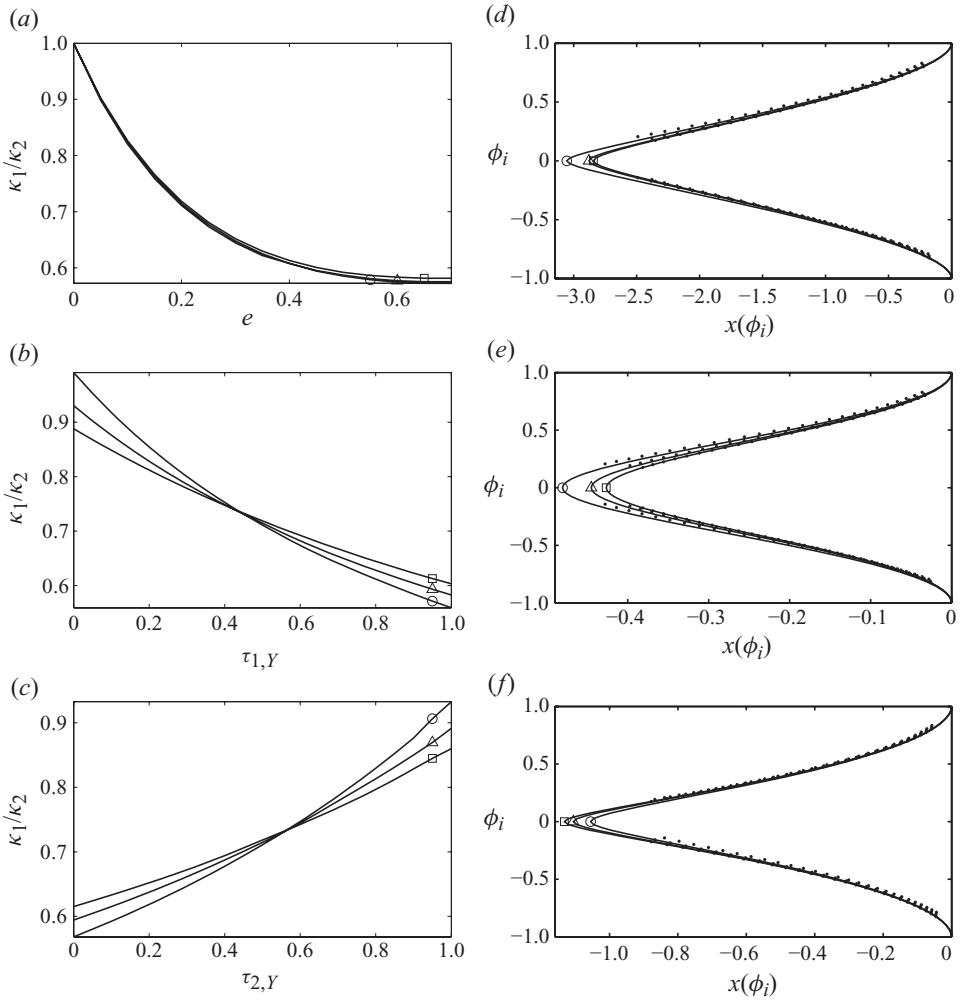

FIGURE 11. (*a–c*) Critical consistency ratio above which we have a steady-state displacement solution: (*a*) κ_1/κ_2 versus e, with $\tau_{1,Y} = 0.5, \tau_{2,Y} = 0.5$; (*b*) κ_1/κ_2 versus $\tau_{1,Y}$ with $e = 0.2$, $\tau_{2,Y} = 0.1$; (*c*) κ_1/κ_2 versus $\tau_{2,Y}$ with $e = 0.2$, $\tau_{1,Y} = 0.5$. Other model parameters are $v_C = -0.5, \alpha = 0$, and in each figure we plot $w_C = -0.5$ (□), 0 (△), 0.5 (○). (*d–e*) Sample steady-state shapes (solid lines) and with first-order asymmetric corrections (dotted lines): (*d*) $\kappa_1/\kappa_2 = 0.83, \tau_{1,Y} = 0.5, \tau_{2,Y} = 0.5, e = 0.1$; (*e*) $\kappa_1/\kappa_2 = 0.95, \tau_{1,Y} = 0.8, \tau_{2,Y} = 0.1, e = 0.2$; (*f*) $\kappa_1/\kappa_2 = 0.85, \tau_{1,Y} = 0.5, \tau_{2,Y} = 0.8, e = 0.2$. In each figure we plot $w_C = -0.5$ (□), 0 (△), 0.5 (○). Other model parameters are $\tilde{b} = -100$.

casing rotation appears to elongate the interface, perhaps via shear-thinning effects. In figure 10(*c*), where the displacing fluid yield stress is smaller than that of the displaced fluid, casing rotation results in a shorter interface.

Figure 11 shows analogous results to figure 10, but for casing reciprocation. We observe again that casing reciprocation has an apparently larger effect than casing rotation on the conditions for there to be a steady states. However, the effects of w_C on length of the steady states appears to be more subdued than those of v_C. We again find the trend of elongation of the steady-state profile with increasing w_C.

5. Discussion and conclusions

In this paper we have formulated a Hele-Shaw model for displacement flows along narrow eccentric annuli, in the case where the inner cylinder is moving, and where the fluids are shear thinning with a yield stress. The resulting quasi-linear elliptic partial differential equation for the stream function has not been solved, primarily due to the complexity of the closure relations between flow rate and modified pressure gradient, in the presence of wall motion. This complexity translates into a heavy computational burden.

Part of the contribution of this paper is in characterizing the closure problem, deriving qualitative results satisfied by the closure functionals and in proposing an efficient algorithm with which to solve the closure problem computationally. These results are detailed in the Appendix, and are important not only for the results in this paper but also if one wishes to analyse and solve the fully two-dimensional problem in the future.

The main results of the paper have been in developing a lubrication/thin-film style displacement model and in its analysis. This model focuses on the limit of large $|\tilde{b}|$, in which buoyancy-driven slumping is prevalent. We have been able to show that in this situation, for sufficiently large ratio of displacing fluid consistency to displaced fluid consistency, a steady travelling wave displacement front can be found. The length of the steady interface at leading order varies with all the dimensionless model parameters. An interesting observation is that due to shear-thinning effects, the steady interface can be either longer or shorter in the presence of casing rotation than without. This depends on whether or not the displacing fluid is more or less shear thinning, as well as on the bulk ratio of effective viscosities.

Viewed in a wider context, the large $|\tilde{b}|$ results here complement those in Carrasco-Teja *et al.* (2008) for the fixed inner cylinder, suggesting that motion of the inner cylinder does not drastically change the underlying dynamics of the limit, $|\tilde{b}| \to \infty$. The results in Carrasco-Teja & Frigaard (2009), although only for Newtonian fluids, showed that for $|\tilde{b}| \ll 1$ it was possible to extend the steady-state results of Pelipenko & Frigaard (2004*a*) to the case of casing motion, i.e. again the underlying dynamics appear unchanged.

However, we should not conclude that motion of the inner cylinder is unimportant. First of all, for many of the flows computed in Carrasco-Teja & Frigaard (2009), where $|v_C| \sim |\tilde{b}|$, localized interfacial instabilities led to mixing over short time scales, and over longer times to displacements that had diffuse interfacial region but remained nearly steady. Here too, if we consider sufficiently large v_C, we may expect that local instabilities appear, and the lubrication model becomes invalid. As an example of this, we present in figures 12 and 13 results of a Newtonian fluid displacement for successively larger v_C. We observe that the lubrication model prediction becomes progressively poorer for $v_C > 1$ and eventually we observe a significant shortening of the interface.

Thus, although the semi-analytical solutions in Carrasco-Teja & Frigaard (2009) and here, are valuable in defining what happens at the limits of large and small buoyancy number, at intermediate buoyancy number, much of the complexity of the displacements does depend on transient two-dimensional dynamics, for which computational solution is needed.

In terms of practical consequences, perhaps the most interesting observation is that conditions for steady-state displacements appear to be relatively unaffected by casing rotation. This implies that process design using the simpler fixed casing model of

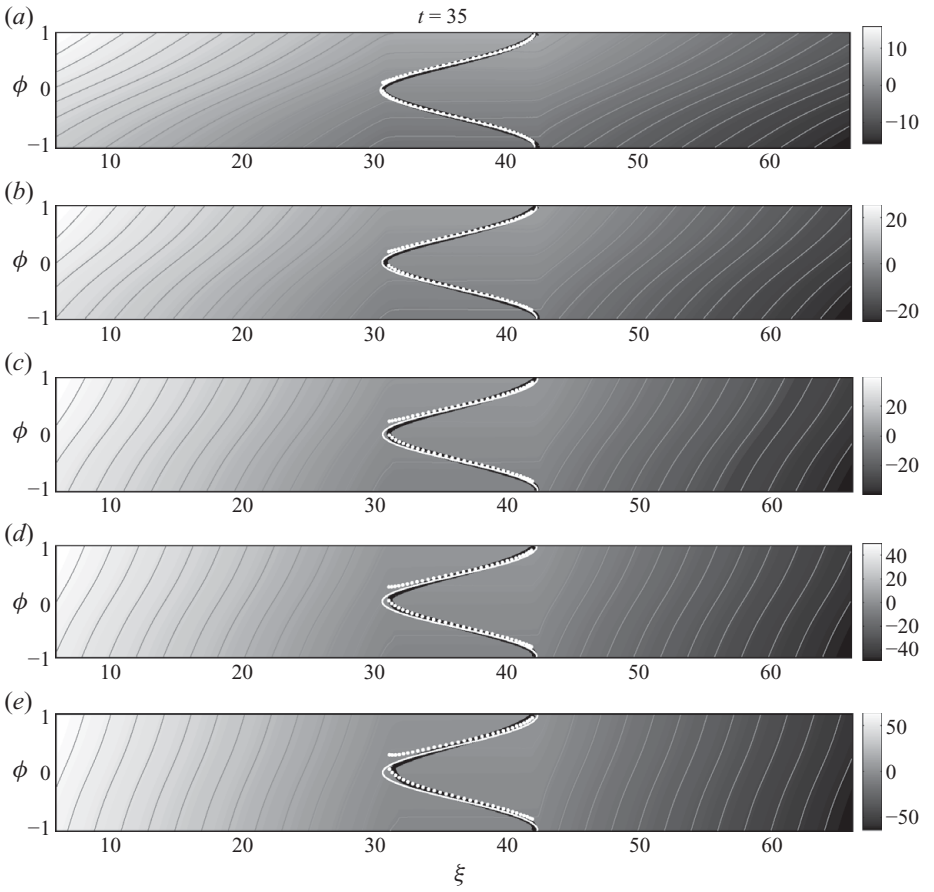

FIGURE 12. The effects of increasing rotation on interfacial stability for two Newtonian fluids; comparison of predicted steady states with numerical computation: (*a*) $v_C = 0.5$; (*b*) $v_C = 1$; (*c*) $v_C = 1.5$; (*d*) $v_C = 2$; (*e*) $v_C = 2.5$. Other parameters are $e = 0.1$, $\kappa_1 = 1$, $\kappa_2 = 0.25$, $\alpha = 0$, $w_C = 0$, $\tilde{b} = -50$ ($\rho_1 = 1$, $\rho_2 = 0.9$, $St^* = 0.002$). See figure 5 for an explanation of the various curves.

Carrasco-Teja *et al.* (2008) may be adequate, simply using casing rotation to ensure that the fluids are yielded/mobilized on the narrow side of the annulus.

From an industrial perspective it may be felt desirable to categorize the effectiveness of the displacement flows in terms of a 'displacement efficiency'. This has been considered but is perhaps an oversimplification that may become misleading. If we consider parameters for which we have a steady state, with axial length of $O(1)$, this is clearly the best situation, with 100 % efficiency. However, beyond that things are less clear. A typical cemented section has dimensionless axial length L of order 10^2–10^4. Therefore, although the asymptotic results here give conditions for steady displacement, the axial lengths of these steady states are of order $|\tilde{b}| \gg 1$. If $|\tilde{b}|$ becomes of the same order as L, then whether or not the steady state is 'useful' becomes an operational or economical question, e.g. (i) is it operationally feasible to pump more of a particular fluid, to ensure that the steady state transits the entire annulus; (ii) in the case that this is possible, are the additional costs of the fluids acceptable. We may just note that the additional volumes needed scale with $|\tilde{b}|$ and material costs are a significant part of the cost of a cementing job. Taking this further,

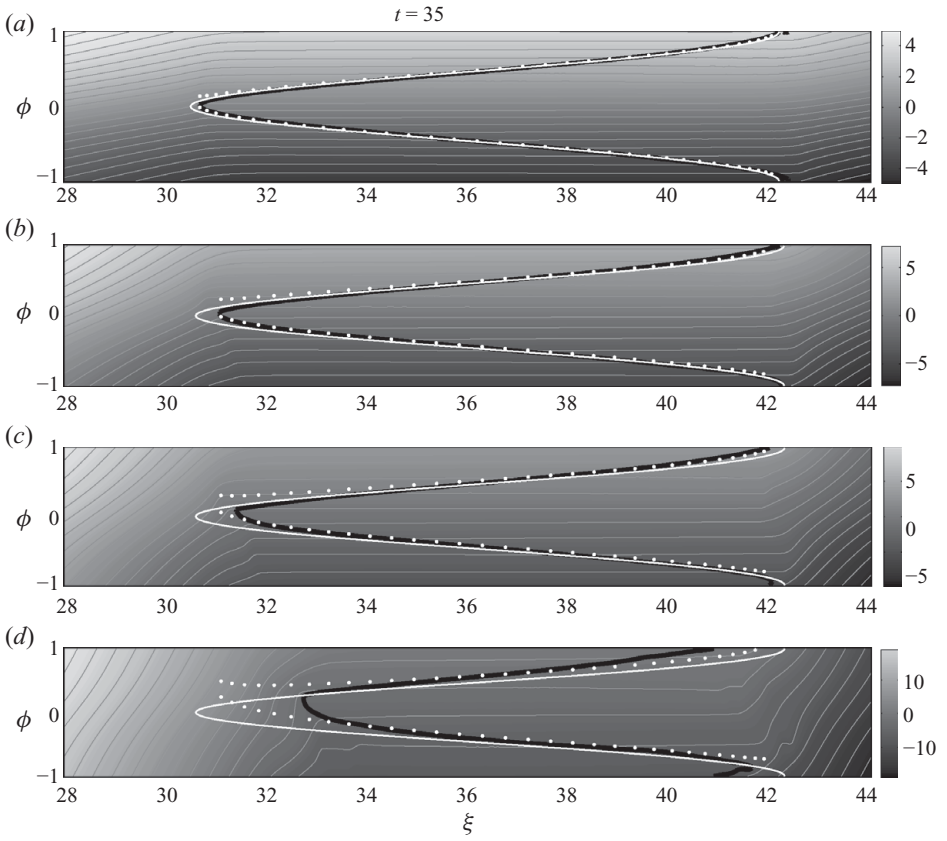

FIGURE 13. Close-up of the interfacial region in figure 12, with parameters: (*a*) $v_C = 0.5$; (*b*) $v_C = 1.5$; (*c*) $v_C = 2.5$; (*d*) $v_C = 5$; (other parameters as before). See figure 5 for an explanation of the various curves.

if $|\tilde{b}|$ exceeds or is comparable to the axial length of the annulus, we must address the question of time scale to achieve the steady state, i.e. if the time required is longer than the residence time in the annulus a steady displacement may not be markedly different from an unsteady displacement. Secondly, once we begin to consider large $|\tilde{b}|$ flows and stratification, questions of stability, mixing and entrainment become important in affecting the efficiency of displacement. Although some progress has been made in this direction (see Moyers-González & Frigaard 2008, 2009), there is still much to be done.

Finally, although it must be acknowledged that the cementing application considered is a rather specialized flow, we should consider the wider fluid mechanical context of the work and its other applications. Firstly, the underlying yield stress fluid models, in the Hele-Shaw context, have a porous media analogue in so-called non-Darcy flows with limiting pressure gradient, i.e. these are nonlinear filtration problems in which yield stress effect is replaced by a critical pressure gradient that must be exceeded. This critical pressure gradient may be either a property of the porous media (e.g. argillaceous soils) or of the fluids flowing in the porous media (e.g. heavy oils). The study of these flows was first carried out by the late V. M. Entov, in the 1970s and subsequently, and is summarized in the two texts: Goldstein & Entov (1989) and Barenblatt, Entov & Ryzhik (1990). In this context, the annular geometry

that we consider corresponds to a spatially periodic anisotropy in the porous media, and with a spatially periodic conservative (gravitational) force field imposed via $\boldsymbol{f}$. For the Couette component in our flows the porous media analogy is unclear to us.

We comment that for porous media studies, it is common to consider geometries in which the displacement fronts are planar or axisymmetric, and the study is focused on, for example, local fingering instabilities. Here, the anisotropy due to eccentricity, the casing motion and the complicated effects of buoyancy and rheology, mean that the underlying steady displacement flow is itself challenging enough to find. We have not even touched on questions of instability and fingering.

Secondly, in the wider application context, we mention that similar Poiseuille–Couette flows occur in annular screw extruders, with narrow gaps and polymeric liquids. Similarly, rotating annular heat exchangers are used in the food industry, where one of the cylinders is often fitted with a scraper system. Here the closure laws are simplified by the assumptions of slow rotation and a dominant axial Poiseuille flow component (see e.g. Fitt & Please 2001). The closure laws that we have developed below in the Appendix are general to these flows and the algorithms suggested have wider utility.

This research has been carried out at the University of British Columbia, supported financially by Schlumberger and NSERC. This support is gratefully acknowledged. We thank B. Seymour for helpful discussions.

Appendix. Closure problem

The closure problem involves finding the relationship between applied pressure gradients and gap-averaged velocity field for a planar two-dimensional shear flow of an Herschel–Bulkley fluid in a plane channel of width $2H$ with the wall at $y=-H$ translating with speed $\boldsymbol{u}_C$. Mathematically, we solve

$$\frac{\partial}{\partial y}\boldsymbol{\tau} = -\boldsymbol{G}, \tag{A 1}$$

where $\boldsymbol{\tau}=(\tau_{\phi y}, \tau_{\xi y})$, $\boldsymbol{G}=(G_\phi, G_\xi)$ and with

$$\boldsymbol{\tau} = \eta(\dot\gamma)\frac{\mathrm{d}}{\mathrm{d}y}\boldsymbol{u} \Longleftrightarrow \tau > \tau_Y, \tag{A 2}$$

$$\dot\gamma = 0 \Longleftrightarrow \tau \leqslant \tau_Y. \tag{A 3}$$

Here we have $\boldsymbol{u}=(v, w)$,

$$\dot\gamma = \left[\left(\frac{\mathrm{d}v}{\mathrm{d}y}\right)^2 + \left(\frac{\mathrm{d}w}{\mathrm{d}y}\right)^2\right]^{1/2}, \quad \tau = \left[\tau_{\phi y}^2 + \tau_{\xi y}^2\right]^{1/2}$$

and

$$\eta = \kappa\dot\gamma^{n-1} + \frac{\tau_Y}{\dot\gamma}.$$

The boundary conditions for $\boldsymbol{u}$ are $\boldsymbol{u}=\boldsymbol{u}_C$ at $y=-H$ and $\boldsymbol{u}=0$ at $y=H$.

Integrating (A 1) gives us $\boldsymbol{\tau}=\boldsymbol{\tau}_0 - y\boldsymbol{G}$, for some unknown stresses, $\boldsymbol{\tau}_0$, at $y=0$. We may note that the velocity gradient is given by

$$\frac{\mathrm{d}}{\mathrm{d}y}\boldsymbol{u} = \frac{1}{\eta(\dot\gamma)}\boldsymbol{\tau} = \frac{1}{\eta(\dot\gamma)}[\boldsymbol{\tau}_0 - y\boldsymbol{G}]. \tag{A 4}$$

From integrating by parts, we have

$$\boldsymbol{u}_C = -\int_{-H}^{H} \frac{\mathrm{d}}{\mathrm{d}y}\boldsymbol{u}\,\mathrm{d}y = \boldsymbol{G}\int_{-H}^{H}\frac{y}{\eta(\dot\gamma)}\,\mathrm{d}y - \boldsymbol{\tau}_0\int_{-H}^{H}\frac{1}{\eta(\dot\gamma)}\,\mathrm{d}y, \tag{A 5}$$

$$2H\bar{\boldsymbol{u}} = \int_{-H}^{H}\boldsymbol{u}\,\mathrm{d}y = H\boldsymbol{u}_C - \int_{-H}^{H} y\frac{\mathrm{d}}{\mathrm{d}y}\boldsymbol{u}\,\mathrm{d}y = H\boldsymbol{u}_C + \boldsymbol{G}\int_{-H}^{H}\frac{y^2}{\eta(\dot\gamma)}\,\mathrm{d}y - \boldsymbol{\tau}_0\int_{-H}^{H}\frac{y}{\eta(\dot\gamma)}\,\mathrm{d}y, \tag{A 6}$$

or alternatively

$$\boldsymbol{u}_C = Hm_1\boldsymbol{G} - m_0\boldsymbol{\tau}_0, \tag{A 7}$$

$$2H\bar{\boldsymbol{u}} = H\boldsymbol{u}_C + H^2m_2\boldsymbol{G} - Hm_1\boldsymbol{\tau}_0, \tag{A 8}$$

for the mobility moments m_j:

$$m_j = \int_{-H}^{H}\left(\frac{y}{H}\right)^j\frac{1}{\eta}\,\mathrm{d}y. \tag{A 9}$$

Rearranging these expressions to eliminate $\boldsymbol{\tau}_0$ leads to (2.21) and (2.22), which reflects the split into Couette and Poiseuille components of the flow. Because the effective viscosity and strain rate appearing in the mobility moments depend on the solution, (2.21) and (2.22) are in fact implicit nonlinear relationships. We turn now to issues of solvability and developing the qualitative understanding of these relationships.

A.1. *Monotonicity results*

For any $\boldsymbol{u}$ and $\boldsymbol{v}\in W^{1,1+n}(-H,H)\times W^{1,1+n}(-H,H)$, define the functionals $a(\boldsymbol{u},\boldsymbol{v})$, $j(\boldsymbol{u})$ and inner product $\langle\boldsymbol{u},\boldsymbol{v}\rangle$, by

$$a(\boldsymbol{u},\boldsymbol{v}) = \int_{-H}^{H}\left|\frac{\mathrm{d}\boldsymbol{u}}{\mathrm{d}y}\right|^{n-1}\frac{\mathrm{d}\boldsymbol{u}}{\mathrm{d}y}\cdot\frac{\mathrm{d}\boldsymbol{v}}{\mathrm{d}y}\,\mathrm{d}y, \tag{A 10}$$

$$j(\boldsymbol{u}) = \int_{-H}^{H}\left|\frac{\mathrm{d}\boldsymbol{u}}{\mathrm{d}y}\right|\,\mathrm{d}y, \tag{A 11}$$

$$\langle\boldsymbol{u},\boldsymbol{v}\rangle = \int_{-H}^{H}\boldsymbol{u}\cdot\boldsymbol{v}\,\mathrm{d}y, \tag{A 12}$$

and let $\mathscr{V}$ be the space:

$$\mathscr{V} = \left\{\boldsymbol{v}\in W^{1,1+n}(-H,H)\times W^{1,1+n}(-H,H) : \boldsymbol{v}(-H) = \boldsymbol{u}_C, \boldsymbol{v}(H) = 0\right\}.$$

Using standard methods, e.g. in Glowinski (1983), we may characterize the closure problem as the following minimization problem:

$$\min_{\boldsymbol{v}\in\mathscr{V}}\frac{\kappa}{n+1}a(\boldsymbol{v},\boldsymbol{v}) + \tau_Y j(\boldsymbol{v}) - \langle\boldsymbol{G}\cdot\boldsymbol{v}\rangle. \tag{A 13}$$

The above functional is strictly convex and the minimization consequently has a unique solution (see e.g. Ekeland & Témam 1976). The solution $\boldsymbol{u}$ also satisfies the following variational inequality:

$$\kappa a(\boldsymbol{u},\boldsymbol{v}-\boldsymbol{u}) + \tau_Y[j(\boldsymbol{v}) - j(\boldsymbol{u})] \geqslant \langle\boldsymbol{G}\cdot(\boldsymbol{v}-\boldsymbol{u})\rangle, \quad \boldsymbol{u}\in\mathscr{V},\ \forall\boldsymbol{v}\in\mathscr{V}. \tag{A 14}$$

For fixed casing velocity $\boldsymbol{u}$, consider two modified pressure gradients, $\boldsymbol{G}_1$ and $\boldsymbol{G}_2$, with velocity solutions $\boldsymbol{u}_1$ and $\boldsymbol{u}_2$, respectively. Evidently the solution space $\mathscr{V}$ is identical for $\boldsymbol{u}_1$ and $\boldsymbol{u}_2$, so that each solution may be used as a test function for the

other. Summing the above variational inequalities for $\boldsymbol{u}_1$ and $\boldsymbol{u}_2$ gives

$$\langle(\boldsymbol{G}_1-\boldsymbol{G}_2)\cdot(\boldsymbol{u}_1-\boldsymbol{u}_2)\rangle \geqslant \kappa[a(\boldsymbol{u}_2,\boldsymbol{u}_2-\boldsymbol{u}_1)+a(\boldsymbol{u}_1,\boldsymbol{u}_1-\boldsymbol{u}_2)] \geqslant 0, \tag{A 15}$$

with the last inequality coming from convexity of $a(\boldsymbol{v},\boldsymbol{v})$. Since $\boldsymbol{G}_1$ and $\boldsymbol{G}_2$ are constant, we have

$$(\boldsymbol{G}_1-\boldsymbol{G}_2)\cdot(\bar{\boldsymbol{u}}_1-\bar{\boldsymbol{u}}_2) \geqslant 0. \tag{A 16}$$

In fact, since $a(\boldsymbol{v},\boldsymbol{v})$ is strictly convex, we have strict inequality above except if $\boldsymbol{u}_1=\boldsymbol{u}_2$.

Suppose that $\boldsymbol{u}_1=\boldsymbol{u}_2\neq 0$. We note that the mobility moments m_j are uniquely defined by $\dot{\gamma}$ and hence by $\boldsymbol{u}$. Thus, in the identity (2.21) we have the same mobility moments for $\boldsymbol{u}_1$ and $\boldsymbol{u}_2$. This implies that either $\boldsymbol{G}_1=\boldsymbol{G}_2$ or the coefficient

$$m_2-m_1^2/m_0=0.$$

However, from the Cauchy–Schwarz inequality we have that $m_1^2 \geqslant m_0 m_2$ with equality only if the integrands of m_0 and m_2 are linearly dependent. However, we observe this can only happen if the integrands are identically zero, i.e. if the effective viscosity is infinite and the fluid unyielded everywhere. But if the casing velocity $\boldsymbol{u}_C\neq 0$, then the fluid cannot be unyielded everywhere. Therefore, we see that the following is true.

(i) If $\boldsymbol{u}_C\neq 0$ then $\boldsymbol{u}_1=\boldsymbol{u}_2$ if and only if $\boldsymbol{G}_1=\boldsymbol{G}_2$. The inequality (A 16) is strict unless $\boldsymbol{u}_1=\boldsymbol{u}_2$, or equivalently, if and only if $\boldsymbol{G}_1=\boldsymbol{G}_2$.

(ii) If $\boldsymbol{u}_C=0$ then $\boldsymbol{u}_1=\boldsymbol{u}_2\neq 0$ if and only if $\boldsymbol{G}_1=\boldsymbol{G}_2$. The inequality (A 16) is strict unless $\boldsymbol{u}_1=\boldsymbol{u}_2\neq 0$, or equivalently, if and only if $\boldsymbol{G}_1=\boldsymbol{G}_2$. Alternatively, if $\boldsymbol{u}_1=\boldsymbol{u}_2$ and $\boldsymbol{G}_1\neq\boldsymbol{G}_2$, then $\boldsymbol{u}_1=\boldsymbol{u}_2=0$.

We note that the latter case corresponds to the fixed casing situation, when indeed different $\boldsymbol{G}$ may lead to $\boldsymbol{u}=0$, provided that $|\boldsymbol{G}|\leqslant\tau_Y/H$.

A.2. *Computation of the closures*

The inequality (A 16) and above comments on monotonicity establish the feasibility of computing the closure. In the case that $\boldsymbol{u}_C\neq 0$ there is a one-to-one mapping between $\boldsymbol{u}$ and $\boldsymbol{G}$, and (A 16) implies that by increasing say G_ϕ we increase u_ϕ and vice versa. Therefore, if we have a 'forward solver' (computing $\boldsymbol{u}$ from $\boldsymbol{G}$), we may use this to iterate monotonically towards finding the correct $\boldsymbol{G}$ that satisfies some constraint $\bar{\boldsymbol{u}}=\bar{\boldsymbol{u}}^*$.

For the purpose of this paper, the type of closure we wish to compute is one in which both $\bar{u}_\phi$ and G_ξ are fixed. Although this could be computed via an outer iteration, as outlined above, one still needs to compute the forward solver. Instead we outline here a method in which the constraints are satisfied within the framework of the forward solver.

Suppose then that $\bar{u}_\phi=\bar{u}_\phi^*$ and $G_\xi=G_\xi^*$. We use G_ϕ as a Lagrange multiplier for the constraint, $\bar{u}_\phi=\bar{u}_\phi^*$, by minimizing

$$\min_{\boldsymbol{v},G_\phi}\frac{\kappa}{n+1}a(\boldsymbol{v},\boldsymbol{v})+\tau_Y j(\boldsymbol{v})-\langle G_\phi(v_\phi-\bar{u}_\phi^*)\rangle-\langle G_\xi^* v_\xi\rangle. \tag{A 17}$$

Again we know that there is a unique solution to this minimization. To cope with the non-differentiability of the above functional, we relax $(\mathrm{d}\boldsymbol{v}/\mathrm{d}y)\mapsto \boldsymbol{q}\in\mathscr{U}=\{L^{1+n}(-H,H)\times L^{1+n}(-H,H)\}$ and replace the above minimization with the

following saddle point problem in the classical way (e.g. Glowinski 1983):

$$\max_{\boldsymbol{s}} \min_{\boldsymbol{v},G_\phi,\boldsymbol{q}} \mathscr{L}(\boldsymbol{v}, G_\phi, \boldsymbol{q}, \boldsymbol{s}), \tag{A 18}$$

$$\mathscr{L}(\boldsymbol{v}, G_\phi, \boldsymbol{q}, \boldsymbol{s}) = \frac{\kappa}{n+1}\langle|\boldsymbol{q}|^{n+1}\rangle + \tau_Y\langle|\boldsymbol{q}|\rangle - \langle G_\phi(v_\phi - \bar{u}^*_\phi)\rangle - \langle G^*_\xi v_\xi\rangle + \frac{r}{2}\left\langle\left(\frac{\mathrm{d}\boldsymbol{v}}{\mathrm{d}y} - \boldsymbol{q}\right)\cdot\left(\frac{\mathrm{d}\boldsymbol{v}}{\mathrm{d}y} - \boldsymbol{q}\right)\right\rangle + \left\langle \boldsymbol{s}\cdot\left(\frac{\mathrm{d}\boldsymbol{v}}{\mathrm{d}y} - \boldsymbol{q}\right)\right\rangle. \tag{A 19}$$

The saddle point problem (A 19) can be solved iteratively using an Uzawa-type algorithm, sequentially determining the optimality for $\boldsymbol{v}$, G_ϕ, $\boldsymbol{q}$ and $\boldsymbol{s}$. This procedure converges under fairly non-restrictive conditions. However, for the problem at hand it does not take full advantage of the known solution structure. Firstly, it is known that in the converged solution: $\boldsymbol{s}\to\boldsymbol{\tau}$ and since $\boldsymbol{\tau}$ satisfies the reduced momentum equations, both components are linear in y. Thus, in place of $\boldsymbol{s}$ we impose

$$\boldsymbol{s} = \tilde{\boldsymbol{\tau}}_0 - y\tilde{\boldsymbol{G}},$$

where $\tilde{G}_\xi = G^*_\xi$, and will iterate to find $\tilde{\boldsymbol{\tau}}_0$ and $\tilde{G}_\phi$ at each step. Evidently, on convergence $\tilde{\boldsymbol{\tau}}_0\to\boldsymbol{\tau}_0$ and $\tilde{G}_\phi\to G_\phi$. Secondly, the problem for $\boldsymbol{v}$ is linear and we might hope to implement the constraint $\bar{u}_\phi = \bar{u}^*_\phi$ directly within the solver, thus determining G_ϕ directly at each iterate. Lastly, we note that for the closure problem, we have no direct interest in $\boldsymbol{u}$, but only in the averaged value $\bar{\boldsymbol{u}}$. Therefore, it appears that there is some wasted effort in computing $\boldsymbol{u}$ at each iterate. We now use these observations, in deriving an improved Uzawa-type algorithm for the saddle point problem.

First let us suppose that an initial guess for $\tilde{\boldsymbol{\tau}}_0$, $\tilde{G}_\phi$ and $\boldsymbol{q}$ is available at step k, say $\tilde{\boldsymbol{\tau}}_0 = \tilde{\boldsymbol{\tau}}^k_0$, $\tilde{G}_\phi = \tilde{G}^k_\phi$ and $\boldsymbol{q} = \boldsymbol{p}^k$. The optimality condition for $\boldsymbol{v}$, which defines $\boldsymbol{u}^{k+1}$, is simply

$$r\frac{\mathrm{d}^2}{\mathrm{d}y^2}\boldsymbol{u}^{k+1} = r\frac{\mathrm{d}}{\mathrm{d}y}\boldsymbol{p}^k - \left(G^{k+1}_\phi, G^*_\xi\right) - \frac{\mathrm{d}}{\mathrm{d}y}\boldsymbol{s}^k = r\frac{\mathrm{d}}{\mathrm{d}y}\boldsymbol{p}^k - \left(G^{k+1}_\phi - \tilde{G}^k_\phi, 0\right).$$

Integrating twice and using the boundary conditions at $y = \pm H$, we find

$$\frac{\mathrm{d}}{\mathrm{d}y}\boldsymbol{u}^{k+1} = -\frac{1}{2H}\boldsymbol{u}_C + \boldsymbol{p}^k - \bar{\boldsymbol{p}}^k - \frac{y}{r}\left(G^{k+1}_\phi - \tilde{G}^k_\phi, 0\right),$$

$$\boldsymbol{u}^{k+1} = \frac{H-y}{2H}\boldsymbol{u}_C + \int_{-H}^{y}\boldsymbol{p}^k(\tilde{y}) - \bar{\boldsymbol{p}}^k\,\mathrm{d}\tilde{y} - \frac{y^2-H^2}{2r}\left(G^{k+1}_\phi - \tilde{G}^k_\phi, 0\right),$$

$$\bar{\boldsymbol{u}}^{k+1} = \frac{1}{2}\boldsymbol{u}_C - \frac{1}{2H}\int_{-H}^{H}\tilde{y}[\boldsymbol{p}^k(\tilde{y}) - \bar{\boldsymbol{p}}^k]\,\mathrm{d}\tilde{y} + \frac{H^2}{3r}\left(G^{k+1}_\phi - \tilde{G}^k_\phi, 0\right),$$

where we have used the notation, e.g.

$$\bar{\boldsymbol{p}}^k = \frac{1}{2H}\int_{-H}^{H}\boldsymbol{p}^k(\tilde{y})\,\mathrm{d}\tilde{y}.$$

Therefore, at the $(k+1)$st iterate we set

$$G^{k+1}_\phi = \tilde{G}^k_\phi + \frac{3r}{H^2}\left[\bar{u}^*_\phi - \frac{1}{2}v_C + \frac{1}{2H}\int_{-H}^{H}\tilde{y}\left[p^k_\phi(\tilde{y}) - \bar{p}^k_\phi\right]\mathrm{d}\tilde{y}\right], \tag{A 20}$$

$$\bar{u}^{k+1}_\xi = \frac{1}{2}w_C - \frac{1}{2H}\int_{-H}^{H}\tilde{y}\left[p^k_\xi(\tilde{y}) - \bar{p}^k_\xi\right]\mathrm{d}\tilde{y}, \tag{A 21}$$

so that the imposed constraint on $\bar{u}_\phi$ is automatically satisfied by this choice of G^{k+1}_ϕ.

The optimality condition for $\boldsymbol{q}$, which defines $\boldsymbol{p}^{k+1}$, consists of minimizing over $\boldsymbol{q}$ the following functional, $K(\boldsymbol{q})$:

$$K(\boldsymbol{q}) = \frac{\kappa}{n+1}|\boldsymbol{q}|^{n+1} + \frac{r}{2}|\boldsymbol{q}|^2 + \tau_Y|\boldsymbol{q}| - \boldsymbol{c}^k \cdot \boldsymbol{q},$$

$$\boldsymbol{c}^k = r\frac{\mathrm{d}}{\mathrm{d}y}\boldsymbol{u}^{k+1} + \boldsymbol{s}^k = r[\boldsymbol{p}^k - \bar{\boldsymbol{p}}^k] - \frac{r}{2H}\boldsymbol{u}_C - y\big(G_\phi^{k+1}, G_\xi^*\big) + \tilde{\boldsymbol{\tau}}_0^k.$$

Note that $\boldsymbol{c}^k = \boldsymbol{c}^k(y)$, so that the minimization of $K(\boldsymbol{q})$ is carried out for $y \in [-H, H]$. We have the following solution:

$$\boldsymbol{p}^{k+1} = 0, \quad \Leftrightarrow \quad |\boldsymbol{c}^k| \leqslant \tau_Y, \tag{A 22}$$

$$\boldsymbol{p}^{k+1} = \frac{|\boldsymbol{p}^{k+1}|}{|\boldsymbol{c}^k|}\boldsymbol{c}^k, \quad \Leftrightarrow \quad |\boldsymbol{c}^k| > \tau_Y, \tag{A 23}$$

$$\kappa|\boldsymbol{p}^{k+1}|^n + r|\boldsymbol{p}^{k+1}| = |\boldsymbol{c}^k| - \tau_Y. \tag{A 24}$$

This last equation requires computational solution if $n \neq 1$, but for the case of a Bingham fluid we see that $\boldsymbol{p}^{k+1}(y)$ is specified as a simple algebraic function at each iterate.

Finally, we update $\tilde{\boldsymbol{\tau}}_0^k$ and $\tilde{G}_\phi^k$ by setting

$$\tilde{G}_\phi^{k+1} = G_\phi^{k+1}, \tag{A 25}$$

$$\tilde{\boldsymbol{\tau}}_0^{k+1} = \tilde{\boldsymbol{\tau}}_0^k - \rho\left[\bar{\boldsymbol{p}}^{k+1} + \frac{1}{2H}\boldsymbol{u}_C\right]. \tag{A 26}$$

The last of these comes from the usual update for $\boldsymbol{s}$, i.e.

$$\boldsymbol{s}^{k+1} = \boldsymbol{s}^k + \rho\left[\frac{\mathrm{d}}{\mathrm{d}y}\boldsymbol{u}^{k+1} - \boldsymbol{p}^{k+1}\right].$$

On substituting for the linear form of $\boldsymbol{s}$ we observe that $\tilde{\boldsymbol{\tau}}_0$ is the mean value of $\boldsymbol{s}$. Substituting from the expression for $(\mathrm{d}/\mathrm{d}y)\boldsymbol{u}^{k+1}$ and averaging over $[-H, H]$ leads to the above projection for $\tilde{\boldsymbol{\tau}}_0^k$.

The parameters r and ρ above are the usual numerical parameters of the Uzawa algorithm. In order to implement this algorithm we use the Newtonian solution to give the initial iterate, $k = 1$. After some algebra this gives

$$\tilde{\boldsymbol{\tau}}_0^1 = -\frac{\kappa}{2H}\boldsymbol{u}_C, \quad \tilde{G}_\phi^1 = \frac{3\kappa}{H^2}\left[\bar{u}_\phi^* - \frac{v_C}{2}\right], \quad \boldsymbol{p}^1 = -\frac{1}{2H}\boldsymbol{u}_C - \frac{y}{\kappa}\big(\tilde{G}_\phi^1, G_\xi^*\big).$$

A.2.1. *Comments*

There are alternatives to the above closure algorithm. However, it is worth noting that for the non-Newtonian fluids, all require some form of numerical integration across the interval $[-H, H]$ as well as some iteration to find the solution. In this sense we can expect that computational times will all be comparable. The advantage of the above approach is that we have not computed the velocity field pointwise in $[-H, H]$ and that the constraints on the mean velocity and modified pressure gradient could be easily incorporated into the algorithm.

REFERENCES

Barenblatt, G. I., Entov, V. M. & Ryzhik, V. M. 1990 *Theory of Fluid Flows Through Natural Rocks. Theory and Applications of Transport in Porous Media*, vol. 3. Kluwer.

Bittleston, S. H., Ferguson, J. & Frigaard, I. A. 2002 Mud removal and cement placement during primary cementing of an oil well; laminar non-Newtonian displacements in an eccentric Hele-Shaw cell. *J. Engng Maths* **43**, 229–253.

Carrasco-Teja, M. & Frigaard, I. A. 2009 Displacement flows in horizontal, narrow, eccentric annuli with a moving inner cylinder. *Phys. Fluids* **21**, 073102.

Carrasco-Teja, M., Frigaard, I. A., Seymour, B. R. & Storey, S. 2008 Viscoplastic fluid displacements in horizontal narrow eccentric annuli: stratification and travelling waves solutions. *J. Fluid Mech.* **605**, 293–327.

Dutra, E., Naccache, M., Souza-Mendes, P., Souto, C., Martins, A. & de Miranda C. 2004 Analysis of interface between Newtonian and non-Newtonian fluids inside annular eccentric tubes. In *Proceedings of ASME-IMECE*, Anaheim, CA. Paper number 59335.

Ekeland, I. & Témam, R. 1976 *Convex Analysis and Variational Problems*. North-Holland.

Fitt, A. D. & Please, C. P. 2001 Asymptotic analysis of the flow of shear-thinning foodstuffs in annular scraped heat exchangers *J. Engng Maths* **39**, 345–366.

Goldstein, R. V. & Entov, V. M. 1989 *Qualitative Methods in Continuum Mechanics*. Academic Press.

Glowinski R. 1983 *Numerical Methods for Nonlinear Variational Problems*. Springer.

Jakobsen, J., Sterri, N., Saasen, A., Aas, B., Kjosnes, I. & Vigen, A. 1991 Displacements in eccentric annuli during primary cementing in deviated wells. *Soc. Petrol. Engrs*. Paper number SPE 21686.

Martin, M., Latil, M. & Vetter, P. 1978 Mud displacement by slurry during primary cementing jobs – predicting optimum conditions. *Soc. Petrol. Engrs*. Paper number SPE 7590.

McLean, R. H., Manry, C. W. & Whitaker, W. W. 1966 Displacement mechanics in primary cementing. *Soc. Petrol. Engrs*. Paper number SPE 1488.

Moyers-González, M. A. & Frigaard, I. A. 2008 Kinematic instabilities in two-layer eccentric annular flows. Part 1. Newtonian fluids. *J. Engng Maths* **62**, 103–131.

Moyers-González, M. A. & Frigaard, I. A. 2009 Kinematic instabilities in two-layer eccentric annular flows. Part 2. Shear thinning and yield stress effects *J. Engng Maths* **65**, 25–52.

Moyers-González, M. A., Frigaard, I. A., Scherzer, O. & Tsai, T.-P. 2007 Transient effects in oilfield cementing flows: qualitative behaviour *Eur. J. Appl. Maths* **18**, 477–512.

Nelson, E. B. & Guillot, D. 2006 *Well Cementing,* 2nd edn. Schlumberger Educational Services.

Nguyen, Q. D., Deawwanich, T., Tonmukayakul, N., Savery, M. R. & Chin, W. 2008 Flow visualization and numerical simulation of viscoplastic fluid displacements in eccentric annuli. In *AIP Conference Proceedings: XVth International Congress on Rheology: The Society of Rheology 80th Annual Meeting*, Monterey, CA, July 7, 2008, vol. 1027, pp. 279–281, doi:10.1063/1.2964662.

Payne, M. L., Wilton, B. S. & Ramos, G. G. 1995 Recent advances and emerging technologies for extended reach drilling. *Soc. Petrol. Engrs*. Paper number SPE 29920.

Pelipenko, S. & Frigaard, I. A. 2004*a* On steady state displacements in primary cementing of an oil well. *J. Engng Maths* **48** (1), 1–26.

Pelipenko, S. & Frigaard, I. A. 2004*b* Two-dimensional computational simulation of eccentric annular cementing displacements. *IMA J. Appl. Maths* **64** (6), 557–583.

Pelipenko, S. & Frigaard, I. A. 2004*c* Visco-plastic fluid displacements in near-vertical narrow eccentric annuli: prediction of travelling wave solutions and interfacial instability. *J. Fluid Mech.* **520**, 343–377.

Sabins, F. L. 1990 Problems in cementing horizontal wells. *J. Pet. Technol.* **42** (4), 398–400.

Savery, M., Darbe, R. & Chin, W. 2007 Modeling fluid interfaces during cementing using a 3D mud displacement simulator. *Offshore Tech. Conf.* Paper number 18513. Curran Associates, Inc., ISBN 9781604231465.

Szabo, P. & Hassager, O. 1995 Simulation of free surfaces in 3-D with the arbitrary Lagrange–Euler method. *Intl J. Numer. Methods Engng* **38**, 717–734.

Szabo, P. & Hassager, O. 1997 Displacement of one Newtonian fluid by another: density effects in axial annular flow. *Intl J. Multiphase Flow* **23**, 113–129.

Tehrani, A., Ferguson, J. & Bittleston, S. H. 1992 Laminar displacement in annuli: a combined theoretical and experimental study. *Soc. Petrol. Engrs.* Paper number SPE 24569.

Vefring, E. H., Bjorkevoll, K. S., Hansen, S. A., Sterri, N., Saevareid, O., Aas, B. & Merlo, A. 1997 Optimization of displacement efficiency during primary cementing. *Soc. Petrol. Engrs.* Paper number SPE 39009.